2024

Visual Experience Enhancement in Augmented Reality Displays

Qian Yang
University of Central Florida

VISUAL EXPERIENCE ENHANCEMENT IN AUGMENTED REALITY DISPLAYS

by

QIAN YANG
B.S. Nanjing University, 2017
M.S. University of Rochester, 2019

A dissertation submitted in partial fulfillment of the requirements
for the degree of Doctor of Philosophy
in the College of Optics and Photonics
at the University of Central Florida
Orlando, Florida

Spring Term
2024

Major Professor: Shin-Tson Wu

ABSTRACT

In the dynamic arena of display technology, augmented reality (AR) displays represent a pivotal advancement, seamlessly bridging the digital and physical worlds. This dissertation delves into the realm of AR display technologies, spotlighting the challenges and limitations of current systems, including transparent and near-eye displays, and proposes innovative solutions to enhance user experience and display performance. With a focus on overcoming issues such as diffraction-induced image blur, the trade-off between resolution and field of view (FoV) in near-eye displays, and FoV constraints in waveguide-based displays, this research introduces new evaluation methods, optimization techniques, and system designs. First, the dissertation presents a quantitative evaluation of diffraction effects on background objects, leading to the development of a pixel structure optimization method aimed at reducing diffraction in transparent displays with small aperture ratios. This advancement promises to enhance image clarity and visibility, addressing one of the key challenges in the deployment of AR technology for transparent displays. Next, we introduce a novel Maxwellian-type foveated AR system that leverages a single light engine. This system employs a temporal polarization-multiplexing method to encode both high-resolution foveal and low-resolution peripheral images through the same light engine. With the aid of polarization-selective lenses, this system effectively separates the two views, delivering a wide FoV and high angular resolution in the foveal region, effectively minimizing the resolution-FoV compromise in near-eye displays. Furthermore, the dissertation conducts a detailed analysis of FoV limitations in single-layer waveguides, proposing a strategic combination of a gradient-pitch polarization volume grating (PVG) with a butterfly exit-pupil expansion

(EPE) scheme. This approach aims to extend the FoV in single-layer waveguides towards the theoretical full-color limit. This research addresses pivotal challenges in waveguide-based AR technology, marking a significant step towards realizing more immersive and user-friendly AR systems.

To my beloved family

ACKNOWLEDGMENTS

I am profoundly grateful for the opportunity to pursue my Ph.D. degree, a journey that has been both challenging and immensely rewarding. Over the past five years, I have been fortunate to receive support and encouragement from many quarters, for which I am overwhelmed with gratitude.

At the forefront of my academic journey, my advisor, Prof. Shin-Tson Wu, deserves my deepest appreciation. His mentorship has been instrumental in my development, both academically and personally. The wisdom he imparted, and the kindness shown by both him and his better half, Cho-Yan Hsieh, have instilled in me with the confidence and resilience necessary for my research and life beyond academia.

My gratitude extends to my dissertation committee members, Prof. M. G. “Jim” Moharam, Prof. Patrick L. LiKamWa, and Prof. Yajie Dong. Their insightful feedback and stimulating discussions have significantly broadened my perspectives and enriched my research experience.

The camaraderie within my research group has been a source of both inspiration and support. Special mention goes to Dr. En-Lin Hsiang and Dr. Yannanqi Li, whose guidance has been invaluable, not only in academic matters but also in navigating my professional path. My heartfelt thanks to all members of the group for their encouragement and collaboration: Dr. Yuge Huang, Dr. Fangwang Gou, Dr. Tao Zhan, Dr. Ziqian He, Dr. Kun Yin, Dr. Jianghao Xiong, Dr. Junyu Zou, Zhiyong Yang, Yuqiang Ding, Zhenyi Luo, Yizhou Qian, John Semmen, Hosna Tajvidi Safa, Yongziyan Ma, Kevin Nilsen, and Keana Paredes.

I am also indebted to Dr. Ming-Yang Deng, Dr. Po-Cheng Lai, Chia-Lun Lee, and Sung-Chun Chen from National Cheng Kung University for their exceptional teachings on display driving circuits, which have greatly enhanced my understanding and skills in this area.

My internship at Apple stands out as a highlight of my journey, providing not only invaluable experience but also the support of remarkable colleagues. I am particularly grateful to Dr. Zhibing Ge, Dr. Young Cheol Yang, Dr. Fuyi Yang, Dr. Guanjun Tan, Dr. Şükrü Ekin Kocabaş, Dr. Kiseung Bang, and Dr. Yang Deng for their encouragement and mentorship during this time. Special thanks to Dr. Fuyi Yang for her continuous support and helpful recommendations during my job search.

The unwavering support of my friends at CREOL has been my anchor through the highs and lows of this journey. I am deeply thankful for their understanding, encouragement, and the countless ways they have stood by me: Dr. Zheyuan Zhu, Dr. Yuanhuang Zhang, Dr. Caicai Zhang, Dr. Mengdi Sun, Di Huang, Weiyu Chen, Huizhong Ren, Li Zhang, Kai Hu, Ko-Han Shih, Le Mei Wang, and Xiaotong Wang.

Last, but certainly not least, my heartfelt gratitude goes to my parents, whose unconditional love and support have been my guiding light. Their unwavering belief in me has laid the foundation for all my achievements.

This journey has been a testament to the strength found in community, mentorship, and family support. I am eternally grateful to each person who has been a part of my Ph.D. odyssey.

TABLE OF CONTENTS

LIST OF FIGURES

LIST OF ABBREVIATIONS

ACR	Ambient Contrast Ratio
AR	Augmented Reality
BSDF	Bidirectional Scattering Distribution Function
CL	Collimating Lens
CLC	Cholesteric Liquid Crystal
CMOS	Complementary Metal Oxide Semiconductor
CP	Circularly Polarized
cpd	Cycles Per Degree
DLL	Dynamic Link Library
DLP	Digital Light Processing
EPE	Exit Pupil Expansion
FDTD	Finite Difference Time Domain
FFT	Fast Fourier Transform
FoV	Field of View
H	Horizontally
HDR	High Dynamic Range
HOE	Holographic Optical Element

HUD	Heads Up Display
HVS	Human Visual System
LBS	Laser Beam Scanning
LCD	Liquid Crystal Display
LCOE	Liquid Crystal based Optical Element
LCoS	Liquid Crystal on Silicon
LCP	Left-handed Circularly Polarized
LP	Linear Polarizer
MEMES	Micro Electro Mechanical Systems
MTF	Modulation Transfer Function
NED	Near Eye Display
OLED	Organic Light Emitting Diode
PAL	Polarization Alignment Layer
PAPH	Photo-aligned Polarization Holography
PBD	Pancharatnam-Berry Phase Deflector
PBS	Polarizing Beam Splitter
PG	Polarization Grating
PPD	Pixels Per Degree

PPI	Pixels Per Inch
PR	Polarization Rotator
PSF	Point Spread Function
PSL	Polarization-selective Lens
PVG	Polarization Volume Grating
QWP	Quarter Wave Plate
RCP	Right-handed Circularly Polarized
RCWA	Rigorous Coupled Wave Analysis
SDR	Standard Dynamic Range
SRG	Surface Relief Grating
TIR	Total Internal Reflection
TL	Template Lens
TN	Twisted Nematic
UV	Ultra Violet
V	Vertically
VAC	Vergence-accommodation Conflict
VHG	Volume Holographic Grating
VR	Virtual Reality

μLED	Micro Light Emitting Diode
μOLED	Micro Organic Light Emitting Diode

CHAPTER 1: INTRODUCTION

1.1 Augmented reality displays

Knowledge is power, and it is acquired through the consumption of vast amounts of information. Since the dawn of human history, humans have devised myriad methods to manifest this information, with paper standing out as a transformative invention. However, the invention of flat panel displays in the last century has revolutionized the way we present information. Nowadays, flat panel displays [1] are ubiquitous in our daily lives. This technology encompasses liquid crystal displays (LCDs) and organic light-emitting diode (OLED) displays, which can be seen in our living rooms, on our desks, in our pockets, and even on our wrists. Despite their prevalence, these conventional displays cannot blend digital information with our physical surroundings and their field of view (FoV) is restricted by the panel size.

This limitation has spurred the development of augmented reality (AR) displays, which promise to merge digital and physical realms seamlessly. Unlike the immersive virtual reality (VR) displays, AR displays let ambient light pass through the device instead of blocking it. One solution is to develop transparent flat panel displays [2], which enable multiple users to see the real world through the display. These transparent displays, allowing real-world visibility through high aperture ratios and transparent electrodes, are known as table-top AR displays. This display technology finds versatile applications across a variety of settings, including retail store windows, car windshields for head-up displays (HUDs), and entertainment displays at Disneyland, to name just a few. Another approach is to downsize the flat panel displays to the point where they can be worn on

the head, incorporating optical elements to project virtual images directly to the eyes, while maintaining visibility of the real world. This method employs various types of microdisplays, including micro-LED (μLED), micro organic light-emitting diode (μOLED), liquid crystal on silicon (LCoS), digital light processing (DLP), and laser beam scanning (LBS) technologies. Known as near-eye AR displays [3], these devices are categorized into two principal designs: free space and waveguide-based. Free space AR, akin to traditional optics, utilizes beam splitters, freeform prisms, or holographic optical elements as off-axis lenses to merge digital projections with ambient reality. Waveguide-based AR [4], on the other hand, uses thin waveguides to couple light from a microdisplay into the eye, resulting in a more compact form factor.

1.2 Challenges and motivation

Despite their potential, AR displays face challenges that hinder their widespread adoption. These include diffraction-induced image blur in transparent displays, a resolution versus FoV trade-off in near-eye displays, and full-color FoV constraints in waveguide-based displays. This dissertation aims to enhance AR display viewing experiences by tackling these issues head-on. Through innovative evaluation methods, optimization techniques, and system designs, we seek to push AR technology forward.

Chapter 2 outlines the requirements for human-centric near-eye displays (NEDs), focusing on comfort, immersion, the human eye's architecture, eyebox, FoV, and eye safety. Furthermore, it includes a summary of various AR optical architectures and the development of compact AR light engines. This discussion lays the groundwork for understanding the key elements necessary to develop user-friendly AR displays. Chapter 3 examines the optical properties of liquid crystal devices and their simulation methods,

establishing the foundation for performance-enhancing design innovations. Chapter 4 introduces a quantitative evaluation for diffraction effects, leading to a pixel structure optimization method that reduces diffraction in transparent displays with small aperture ratios. In Chapter 5, a novel Maxwellian-type foveated AR system is proposed, utilizing a single light engine. This system employs temporal polarization-multiplexing method to encode high-resolution foveal and low-resolution peripheral images into the light engine. With polarization-selective lenses, the system separates the two views, achieving a large FoV and high angular resolution in the foveal region. In Chapter 6, a comprehensive examination of FoV limitations in single-layer waveguides across various exit-pupil expansion (EPE) schemes is presented. We delve into the relationship between FoV limitations and the angular response of the waveguide combiner, proposing a groundbreaking approach that combines a gradient-pitch polarization volume grating (PVG) with a butterfly EPE scheme. This strategy aims to maximize the FoV in single-layer waveguides, pushing towards the theoretical full-color FoV limit. Chapter 7 concludes the dissertation, summarizing our contributions to advancing AR display technology.

CHAPTER 2 HUMAN-CENTRIC NEAR-EYE DISPLAYS

2.1 Comfort and immersion

Head-mounted AR/VR devices should be designed in terms of both comfort and immersion [5,6]. Comfort determines how much time a user can wear a NED, while the immersion requires that the display turns the virtuality into reality. The comfort comes with wearability [7], visual experience [8], and social interaction [9]. The immersion relates to all kinds of human senses, especially in aural, visual, and haptic senses [10]. The optics mainly determines the visual comfort and immersion in NEDs [11], but it also plays an essential role for wearable and social comfort. For example, a NED must have a small form factor and lightweight to widen the consumer acceptance [12]. The weight of a headset should be evenly distributed as possible and therefore the center of gravity is close to the head, enabling comfortable wearing for a long-time use. Since optics occupies a larger volume in a near-eye headset, both light engines and combiners should be lightweight and compact as well. Therefore, the first requirement for an advanced light engine is compactness. For an optical see-through AR device, it is expected that a user's eyes can be clearly seen by others, allowing true eye contact for social interaction. Visual comfort and immersion are not easily measurable objective metrics. They are subjective experiences and vary from person to person [13]. Thus, the design of AR/VR devices should be a human-centric task. The human visual system (HVS) has its unique capabilities and limitations. A detailed understanding of HVS helps designers make sensible trade-offs in optical specifications or even reduce the system complexity by taking advantage of HVS.

2.2 Architecture of human eye

The HVS consists of two eyes and the interpupillary distance (IPD) is the distance between the center of two eyes (Fig. 2-1(a)), usually expressed in millimeters. This value (49-76 mm) may vary with each individual [14], depending on age, gender, and ethnicity. An eye is essentially an imaging system including multiple refractive surfaces and an adjustable iris [15]. A simplified eye model is illustrated in Fig. 2-1(b).

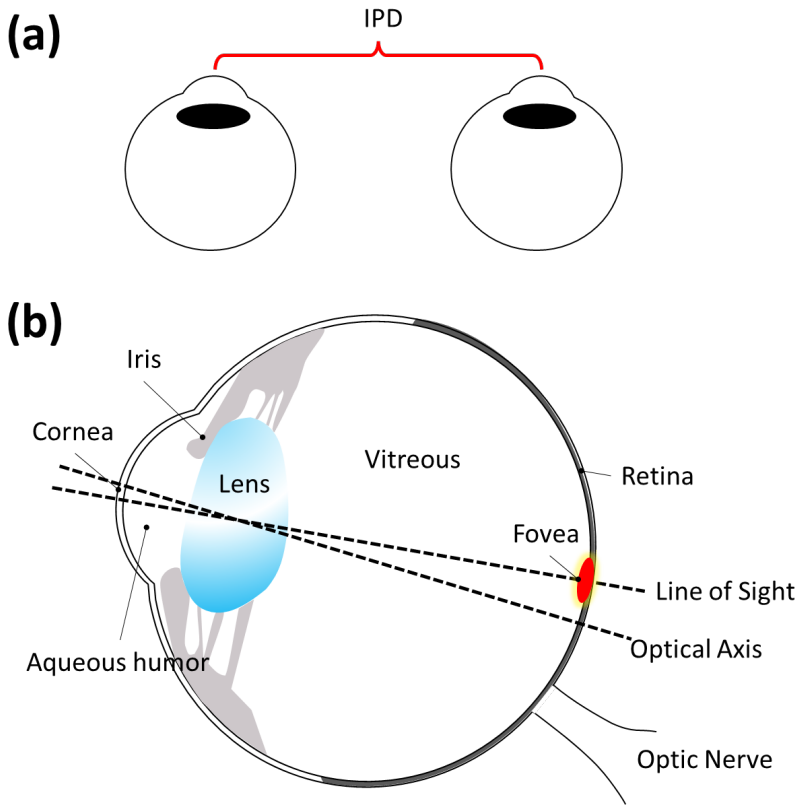

Figure 2 - 1 (a) An Illustration of interpupillary distance (IPD) in humans. (b) A schematic of a simplified human eye model.

The incident light passes through cornea and aqueous humor and then enters the pupil, a round opening in the center of iris. The iris adjusts the effective F number of the imaging system by changing the size of pupil, limiting the light throughput. As light continues, it passes through the lens. The lens is attached to muscles which can change the shape

and optical power of the lens by contracting or relaxing. This feature enables humans to accommodate for an in-focus image at different depths. The last refraction occurs on the interfaces between the lens and vitreous and finally an image is formed on the retina. From there, photoreceptors including cone cells and rod cells convert light intensity into electrical impulses, which are unevenly distributed on the retina. Cone cells concentrate mostly in the central region of the retina called macula, which spans about 5 mm. Visual acuity refers to the ability for a human eye to resolve small features. The fovea, in the center of macula, has the maximum visual acuity due to its highest photoreceptor density, covering only 2-3° [5]. For a 20/20 vision, an eye should be able to resolve detail as small as 1 arcmin, or, in other word, the angular resolution is 60 pixels per degree (PPD) in the fovea. Outside the fovea, visual acuity declines rapidly in the rest region of macula. Rod cells can be found away from the macula, responsible for scotopic vision with low resolution perception. In AR/VR systems, both imaging quality of optics and resolution density of light engines affect the final image quality on the retina. Modulation transfer function (MTF) [16] is an indicator of how well an imaging system can reproduce fine details and sharp edges as shown in Fig. 2-2(a). MTF shows the contrast performance as a function of angular or spatial frequency, and it decides the spatial frequencies which the display and following optics can deliver to an eye. The perceived PPD may be lower than expected if the optics between the display panel and eyes show a poor MTF. Failing to satisfy such a high PPD leads to screen door effect [17], where a mesh pattern is overlaid over the image, like seeing the world through a screen door (Fig. 2-2(b)). The “screen door” is essentially the pixel structure of a display panel as the fill factor is not

100% and only part of a pixel is emitting, transmitting, or reflecting light. Here, we present the second requirement for an advanced display light engine: high resolution density.

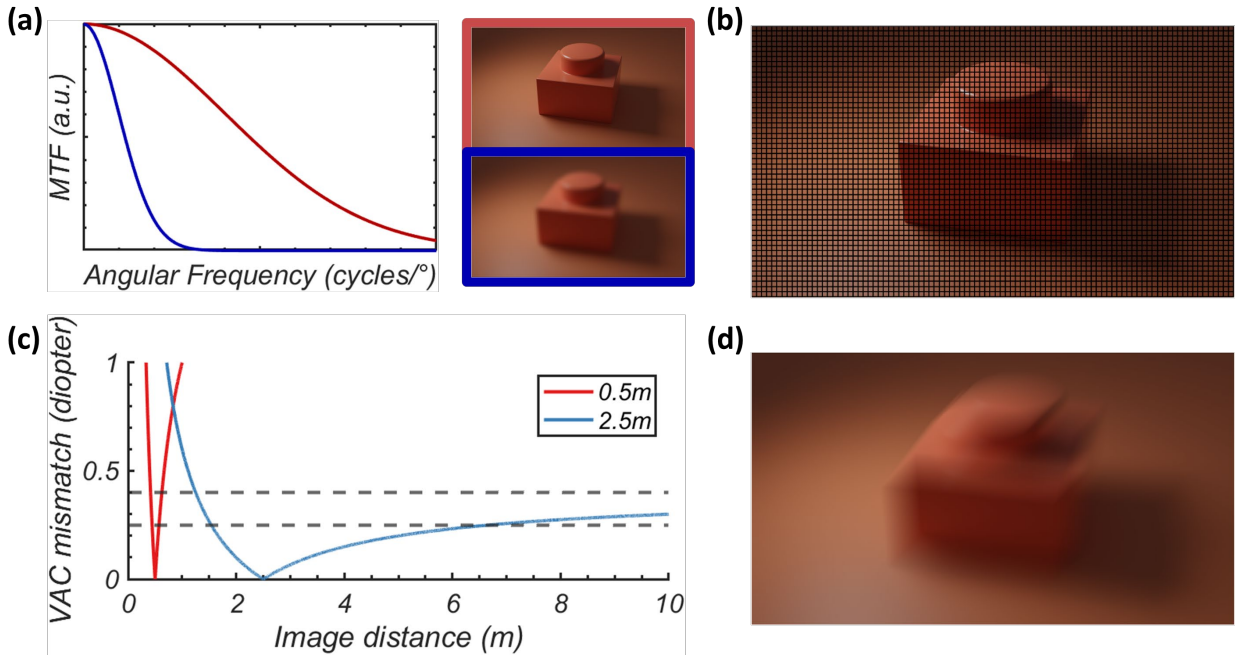

Figure 2 - 2 (a) The impact of excellent (red) and poor (blue) MTF to display quality. (b) A displayed image with screen door effect. (c) Vergence-accommodation tolerances at a near (0.5m) and far (2.5m) distance. (d) A displayed image with motion blur.

The image perceived by human eyes is not a flat 2D image but with 3D sense. Depth cues exist in the HVS [18]. Physiologically speaking, the depth cues include accommodation, convergence, and motion parallax [19]. On one hand, the lens in an eye can dynamically accommodate its shape as well as optical power to form clear images at different depths. On the other hand, with binocular vision, each eyeball will rotate to converge their lines of sight on the focused object. Thus, this convergence angle provides the depth information to the visual cortex. These two depth cues, vergence and accommodation, are closely linked within the HVS and are intrinsically matched with each other in reality. The ability for human eye to perceive the depth variation is called stereo

acuity. The HVS is not sensitive to the depth change caused by absolute distance difference, but by diopter difference [20,21]. This feature tells that the HVS is more sensitive to the depth variation at a close range, usually referred to as 'one-arm's length', which is about 30-50 cm. For objects at a farther range, stereo acuity is not sensitive. When looking at a fixed focus stereo display, a user is forced to accommodate to a single distance to obtain a clear image, but stereoscopic disparity tells eyes to make a vergence for objects at different depths, introducing vergence-accommodation conflict (VAC) [22,23]. The VAC tolerance range for a near and far distance is illustrated in Fig. 2-2(c). If the image plane is set at 2.5 meters away from a user, then the acceptance region covers about 5 m, from 1.5 m to 6.7 m, if the VAC tolerance limit is set to 0.25 diopters. For a higher VAC tolerance limit, say 0.4 diopters, then for 1.25 m to infinity, there is no VAC issue. However, for a closer imaging plane at 0.5 m, the acceptance region will be much narrower due to drastic diopter variation. Integral imaging displays [24,25] and holographic displays [6,26] are proposed to reproduce the light field by ray approximation or a complete wavefront. Maxwellian displays [12,27] avoid VAC by creating a large depth of focus image and may introduce natural blur through image rendering. In light engines with a high frame rate, accompanying with an active combiner, more focal planes [28] can be created statically or dynamically at near depth to mitigate the VAC issue. In addition, motion artifacts [29] in nature usually happens when an observed object or an observer's eye is moving too fast, resulting in an inability to resolve details, as depicted in Fig. 2-2(d). A nature-looking movement requires some degree of motion blur, but if the response time [30] of the hold-type display is not fast enough [31], extra undesired motion artifacts may be caught by the users. Motion artifacts in NEDs may also occur when the head

moves too fast, and the displayed content is not updated synchronously. This is usually described as motion-to-photon latency [32,33]. Fast sensors and better video processing pipelines could also diminish this nausea. Based on the discussion above, we present the third requirement for an advanced display light engine: fast response time.

The HVS has a huge dynamic range, from the dim starlight at 10^{-6} nits to the bright sunlight at 10^{8} nits, as shown in Fig. 2-3. In dark light environments, or at scotopic light levels, it is mainly the rod cells are responsive for luminance ranging from 10^{-6} to 10^{-2} nits, while cone cells are active for photopic light levels (10 to 10^{8} nits). In between these two ranges (mesopic range), both rod and cones are involved in the sensing. The difference in scale between the darkest and brightest objects a human eye can perceive spans 14 orders of magnitude. At one time, the HVS can only perceive a subset of such range, say about 5 orders. The traditional standard dynamic range (SDR) displays cover 3 orders, but high dynamic range (HDR) [34,35] displays aim to match the steady dynamic range of the human eye, allowing objects to be represented with better fidelity to their nature. Human eyes are more sensitive to the illuminance variation at low light levels, so high contrast ratio, lower dark level, and more bits at low gray levels are preferable in HDR displays.

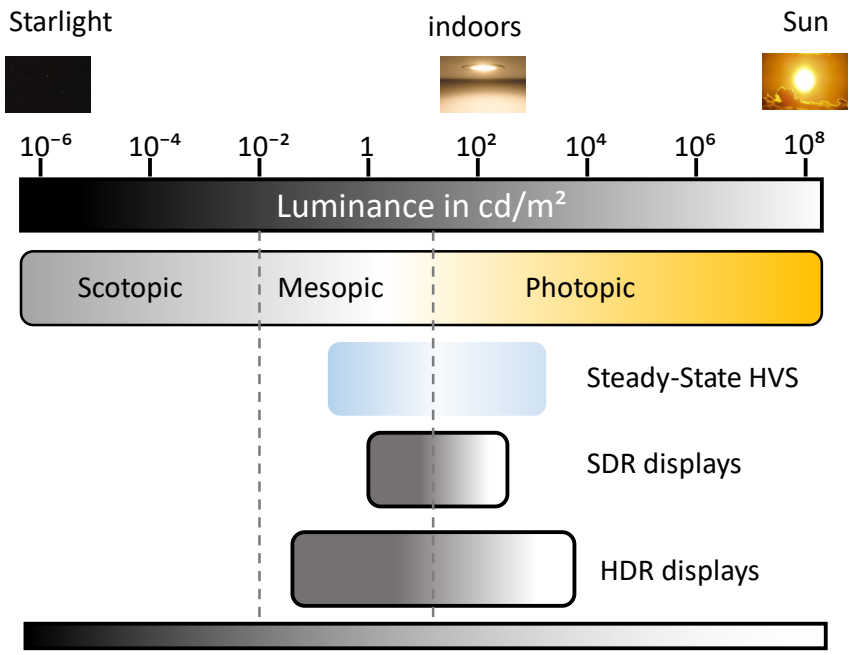

Figure 2 - 3 Dynamic range of the human visual system.

For AR applications, the high illuminance of a HDR display is vital for outdoor scenarios. The ambient contrast ratio (ACR) [36] should achieve at least (3:1) for an acceptable readability. Considering the ambient illuminance is 3,000 nits on a sunny day, the display needs to deliver at least 10,000 nits, regardless the optical loss. If methods like EPE are applied to enlarge the eyebox, an AR device will demand a much higher brightness from the display panel. Due to limited battery capacity the optical efficiency of the overall system should be high. Given the ambient light is fully blocked in VR headsets, 150-200 nits of brightness received by human eye is acceptable after considering the optical losses. Here, we present the fourth and fifth requirements for an advanced display light engine: high dynamic range, high efficiency and peak brightness, and long lifetime.

2.3 Eyebox and FoV

In HVS, an entire FoV spans more than 200° horizontally (H) and about 130° vertically (V), while the binocular overlap is about 120° H, as shown in Fig. 2-4. When eyes are in a relaxing state, steady gaze is possible for a FoV of ±20° H and +15°/-20° V, without producing any eye strain. Compared to horizontal FoV, the vertical FoV is asymmetric since the relaxed line of sight is 15° below the horizontal line of sight. Fig. 2-4 shows capabilities of each part of FoV in HVS.

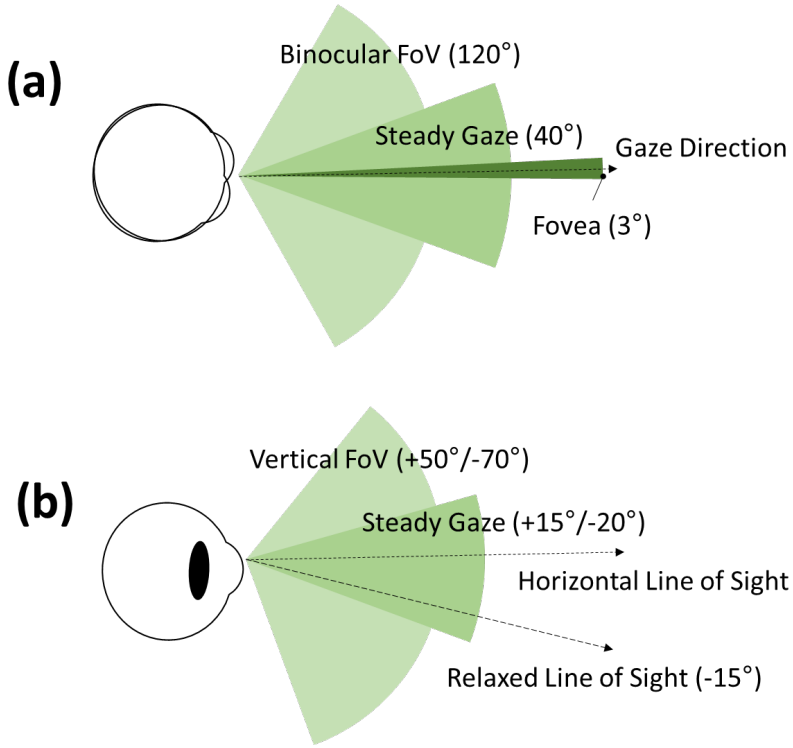

Figure 2 - 4 (a) Horizontal and (b) Vertical human vison FoV.

Eyebox [37] is a physical 3D region where the whole FoV can be viewed without vignetting. In an AR/VR device, this 3D volume is closely related to the exit pupil size of the optical combiner. Although the eyebox is defined in terms of volume, it is usually expressed as a few millimeters horizontally. A larger eyebox would allow an AR/VR device

to be faster set up and better accounted for variations in human IPD and positioning of the head. Eye relief [38] refers to the distance from the last optical surface to the best viewing spot. A shorter eye relief generally increases the perceived eyebox size but may prohibit users from wearing glasses if needed. Also, due to the conservation of Lagrange invariant and étendue in an imaging system, a tradeoff exists between the eyebox and FoV. In AR devices, pupil replication [27,39] and pupil steering [40] techniques are proposed to mitigate the limited eyebox.

2.4 Eye safety

Cone cells on the retina have different spectral sensitivities and are generally labeled by their peak wavelengths as short (S), medium (M), and long (L) cone types. According to the trichromatic theory, the same color can be perceived by a human eye even if the input light spectrum is different, as long as the tristimulus values remain the same. This gives some freedom on the choice of the light sources in AR/VR displays to reproduce the desired colors. However, the designer must take good care of spectrum brightness perceived by human eyes, following the eye safety regulation. For example, at the same brightness, deep blue is more harmful to eyes than light blue. Nowadays, mainstream light sources are LED (both inorganic and organic) and lasers. An LED usually manifests a broader spectrum and therefore has more leakage in UV region than lasers, while lasers may cause severe eye damage if no failure detection protocol is set up.

2.5 Optical architectures of AR displays

AR display architectures are often categorized by their combiners. Based on where the incident light propagates, there are three types of optical combiners: free-space combiners, freeform prism combiners, and waveguide combiners.

2.5.1. Free-space combiner

The simplest free-space combiner is a 50/50 beam splitter. The output light from an optical engine is reflected to the eye while the ambient light from real world passes through the beam splitter and is combined with the display light, as shown in Fig. 2-5(a). Some optical power can be added to the partial reflector by making it a curved surface [41] (Fig. 2-5(b)), enabling a large FoV, but this design suffers from image distortion because all the optical power is provided by a single surface and the form factor is large. The birdbath optics [42] in Fig. 2-5(c) folds the optical path for a smaller form factor and introduces additional optical elements for aberration correction. The above architectures serve as traditional imaging systems, imaging from a 'real' plane of a light engine to a 'virtual' plane. Then this 'virtual' plane is imaged by an eye to the retina. Thus, display panels like OLED, μLED, DLP, and LCoS are preferred. However, in a Maxwellian display [12,27,39,40,43], the combiner reflects the image from the light engine to the eye pupil, as shown in Fig. 2-5(d). Since the focusing spot is much smaller than the eye pupil, a clear image with infinite depth of focus can be formed on the retina, no matter what optical power of the eye is. An LBS display [44] is a natural point source and thus can be directly applied in Maxwellian displays. A spatial light modulator (SLM) like LCoS or DLP [26] can also be used in Maxwellian displays if illuminated by a collimated light, as Fig. 2-5(e) shows. An off-axis holographic optical element (HOE) combiner is preferred in a Maxwellian display for achieving an aberration-free imaging.

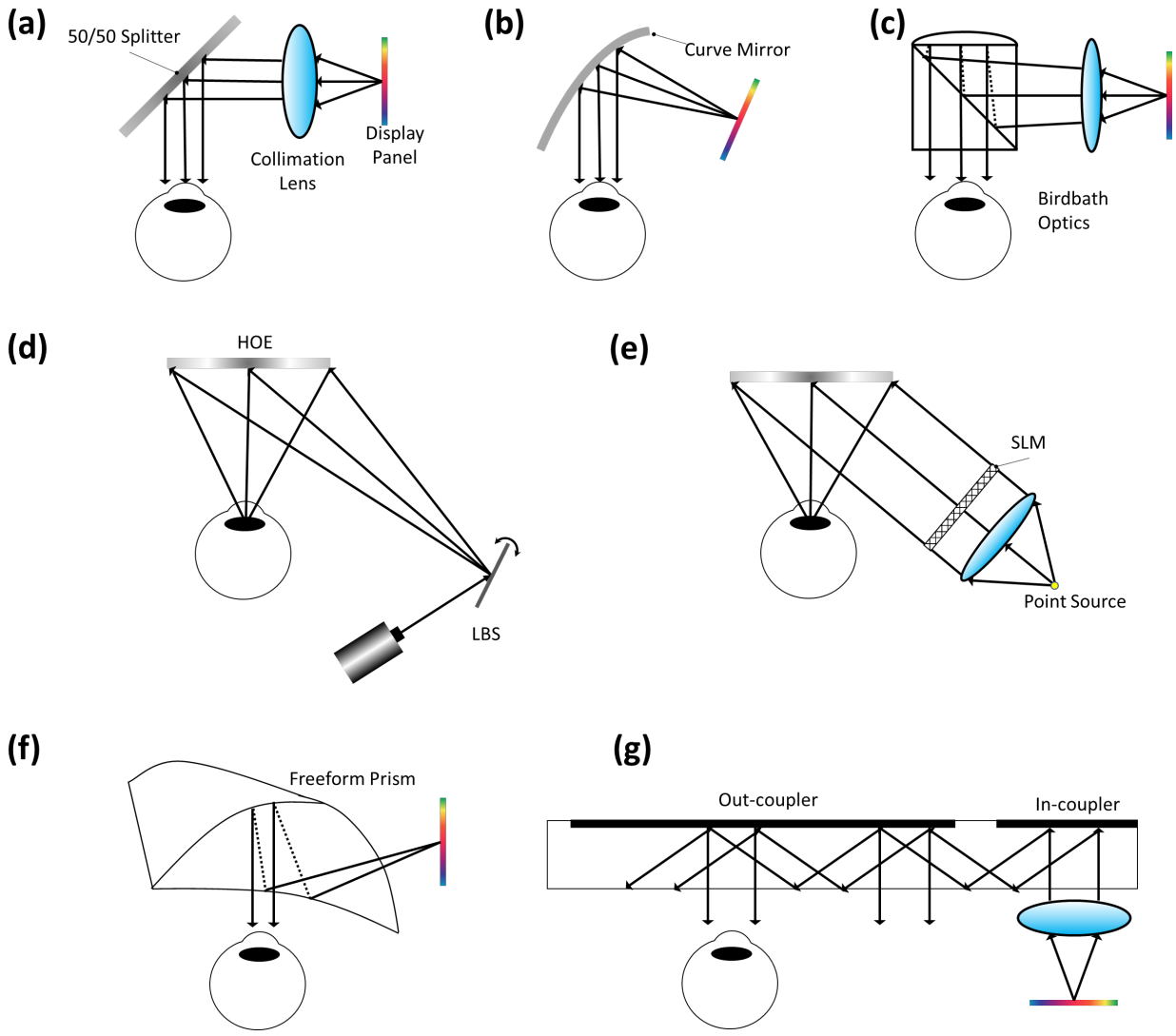

Figure 2 - 5 (a) A 50/50 beam splitter as a combiner. (b) A single reflective curved surface combiner. (c) A birdbath design combiner with a folded optical path. (d) A Maxwellian display based on a LBS. (e) A Maxwellian display based on a SLM. (f) A freeform prism combiner. (g) A waveguide combiner consisting of two reflective type diffractive gratings. HOE: holographic optical element. SLM: spatial light modulator.

2.5.2 Freeform prism and Waveguide combiners

In both freeform prism combiners [45] and waveguide combiners [36], the imaging light propagates in either prism or waveguide by total internal reflection (TIR), as depicted in

Fig. 2-5(f) and Fig. 2-5(g), respectively. The optical path is folded in a prism combiner and each surface is carefully designed for achieving an excellent image quality. The most obvious feature in a waveguide combiner is the EPE process, which breaks the étendue limit and effectively increases the eyebox size. The upper limit of the FoV is determined by the waveguide refractive index, which is about 70° for a n=2 glass. Usually, for a display panel, the output image is first Fourier transformed to far field, converting image information from spatial to angular domain. However, the LBS display does not require such a conversion. Then, display light is coupled into a waveguide, propagates through TIR process, and finally is outcoupled into human eyes. The in- and out-coupler can be a prism, a diffractive grating, or partial reflective mirrors.

2.6 Recent progress on compact AR light engines

Presently, several microdisplay technologies, such as μLED, μOLED, LCoS, DLP, and LBS have been developed for AR. Each technology has its own pros and cons. Fig. 2-6 shows a generic comparison between the volume and the FoV in panel-based displays. Among them, quantum-dot based μLED and μOLED displays are both self-emissive and can achieve very high pixel density and full color on a single panel, which seems ideal for compact light engines. However, the tradeoff between brightness and lifetime remains to be overcome for μOLED to extend its application to AR because of the high brightness requirement [46]. μLED aims to preserve all the advantages of μOLED and mitigate the brightness-lifetime issue, but the mass production is still in the infancy stage [47]. Although these two panel-based display technologies still have limited market penetration in present AR headsets, they remain strong contenders because the above-mentioned issues are gradually overcome. LCoS and DLP are both non-emissive panel displays and

have reached a matured stage for mass production after decades of investments in standard complementary metal–oxide–semiconductor (CMOS) technology [48], but an extra illumination system usually leads to a larger form factor. In the illumination system, the light from an external illuminating source (e.g., LEDs) usually needs to be homogenized by passing through a pair of fly-eye lenses or a rod integrator before reaching the LCoS/DLP panel. In a traditional LCoS display [49], a polarizing beam splitter (PBS) functions as both a polarizer and an analyzer. In the telecentric DLP display [50], a light separator (prism) is employed to direct the uncontrolled beam away from the projection lens. To further reduce the form factor, these bulky optics should be shrunk or even removed. The transmissive LCD, like LCoS, relies on liquid crystal for amplitude modulation, but it uses a backlight illumination. At the first glance, the transmissive property seems intriguing to make a simpler optical design, but the lower fill factor (~20% due to black matrices) limits its pixel density to be ~2000-3000 pixels per inch (PPI), which is lower than its reflective counterpart (>4000 PPI). On the other hand, LBS consisting of a tiny laser module and micro-electro-mechanical systems (MEMS) mirrors, has a very attractive form factor and is still pushing its limit, but its frame rate and scanning uniformity remain to be improved. Next, we will discuss about recent progress in reducing the form factor of LCoS and LBS displays.

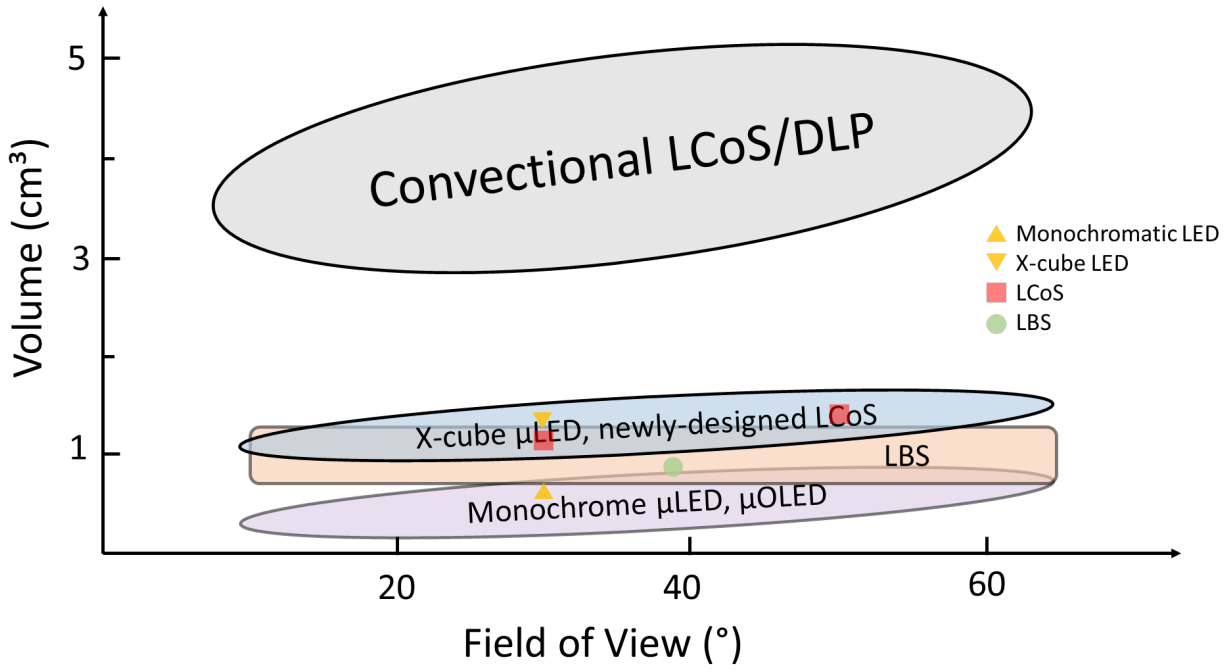

Figure 2 - 6 A qualitative comparison of volume size of each light engines in AR at each field of view. Data points from either prototypes or commercial products are marked out.

A conventional LCoS display consists of a color combiner, a homogenizer, a PBS, and a LCoS panel, as shown in Fig. 2-7(a). This configuration is referred to as free-space-lit LCoS, since light mainly propagates in free space. Similar to the edge-lit backlight [51] for a direct-view LCD, a back-lit LCoS [52] was proposed to reduce to from factor of the illumination system, as plotted in Fig. 2-7(b). The whole illumination system could be replaced by a lightguide plate with LEDs on the edge. The lightguide mixes the input light to attain uniform illumination. Still, a PBS cube, which is about 1 cm^3, is required to polarizing and directing the illumination toward the LCoS panel, and then analyzing the spatially modulated light from the LCoS panel. If the LCoS panel is directly illuminated from top, then the bulky PBS can be replaced by a planar polarizer.

Later, a so-called front-lit LCoS [53,54] is introduced by placing a flat plate in front of LCoS to eliminate both illumination system and PBS, as shown in Fig. 2-7(c). The idea of 'front-lit' could trace back to the reflective LCD direct-view displays [55] in mid-1990s to solve the readability issue in low-light condition. The flat plate is only 1-mm thick in total and the detailed structure of front-lit LCoS is illustrated in Fig. 2-7(d). The front-lit plate contains a lightguide on top of the LCoS module. The LED is located on the edge of the lightguide, and a polarizer is inserted between the LED and the lightguide. On top of the lightguide, a reflective polarizer is placed as an analyzer. Assuming the polarizer attached to the LED transmits s-polarized light, the reflective polarizer should reflect s-wave and let p-wave pass. The s-wave propagates in the lightguide by TIR process or reflecting from optical elements like dielectric mirrors. When the TIR condition is not satisfied, the ray escapes from the lightguide and is modulated and reflected by the LCoS panel. The p-wave in the reflected ray passes the reflective polarizer and forms an image. The downside of this design is that the viewing cone is limited to about 30°. In the original design [53], the LCoS is operating in color-filter mode illuminated by a white LED. If operating in color sequential mode [54], an additional hollow rod is used for RGB color mixing by means of multiple reflections, but the overall thickness of the front-lit plate is still slim (1.5mm).

Recently, a new LCoS architecture [56,57] specially designed for large-FoV AR applications radically removes the light guide in the front-lit design, as shown in Fig. 2-7(e). In this design, the LCoS panel modulates a circularly polarized light. The RGB LEDs are placed side-by-side in the light source region. A reflective polarizer is attached to LEDs for polarization recycling. A linear polarizer (LP) attached with a quarter-wave plate (QWP) converts the incident light to left-handed circularly polarized (LCP) state. A lens is

placed below QWP and functions as a Fourier Transform of the LED light. The LCoS panel at the focal plane of the lens receives the angular spectrum of light from LEDs, where each pixel corresponds to a plane wave component at a different propagation angle. When the light is reflected, the spatial pixel is transformed to far field after passing through the lens for a second time, which is exactly what a waveguide combiner needs. A double circular polarizer, a linear polarizer sandwiched between two crossed QWPs, is inserted between the lens and the LCoS, functioning as a polarizer and analyzer. The orientation of the slow axis of QWP1 and QWP3 should be aligned, while that of QWP2 is orthogonal to the other two. In the on-state, the LCoS panel modulates the incident light so that the polarization state of the reflected light remains unchanged, which is still LCP and passes through two linear polarizers without any loss ideally. The circular polarization helps suppress stray light caused by Fresnel reflection which will flip the handedness of incident light. For example, the stray light is left-handed circularly polarized (RCP) and will be absorbed by the LP1. Such a compact LCoS design shortens the distance between the collimation lens and the waveguide combiner, and therefore enlarges the FoV. With an improved LCoS design, some commercial products with volume close to $1cm^3$ have been launched [58].

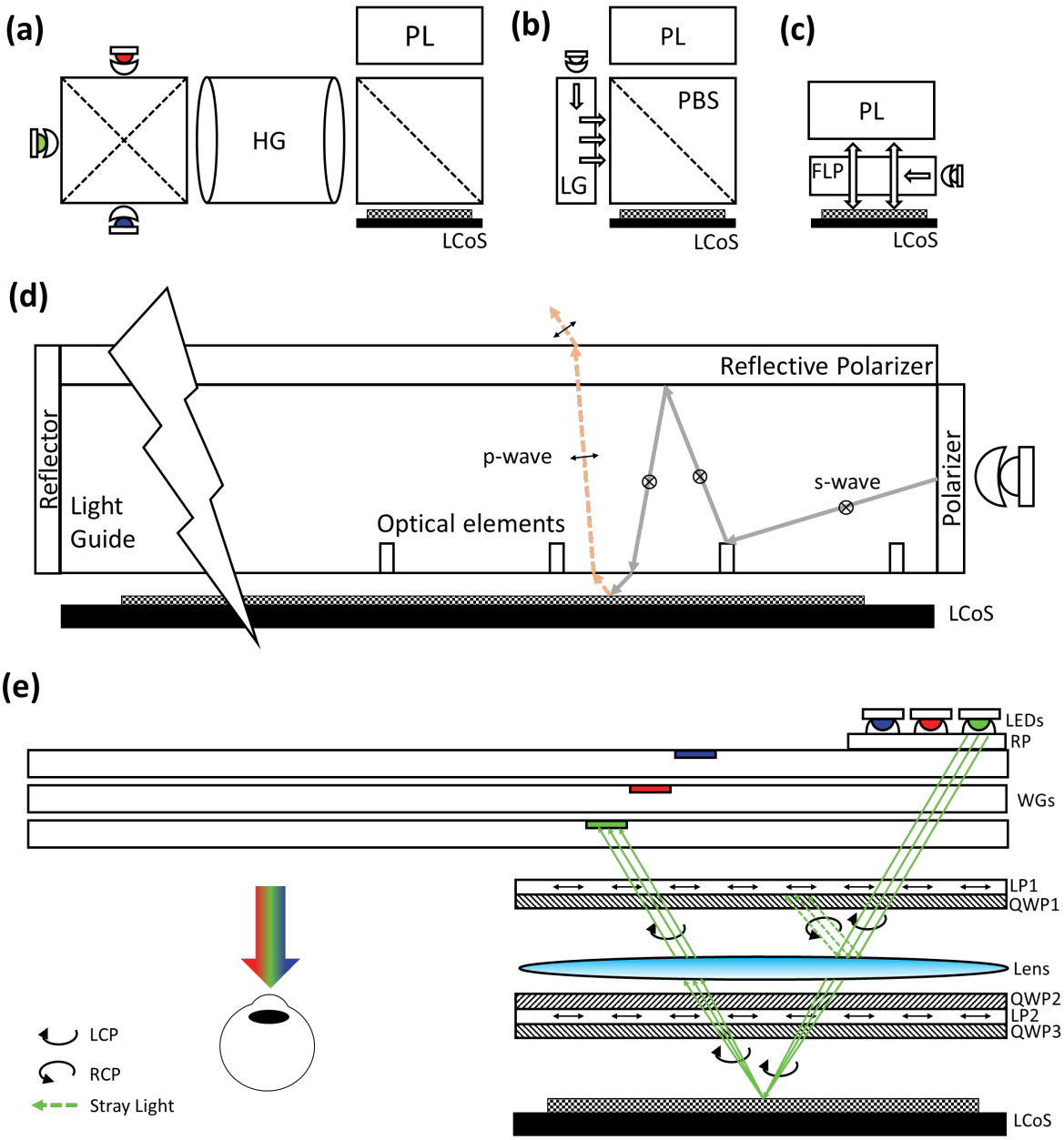

Figure 2 - 7 (a) A free-space color-sequential LCoS design with a X-cube, a homogenizer, and a PBS. (b) A backlit LCoS with collimation optics replaced by a light guide. (c) A front-lit LCoS where the PBS is removed. (d) Light propagation process in a front-lit LCoS. (e) A new slim LCoS with an enlarged FoV. HG: homogenizer. PL: projection light. LG: light guide. FLP: front-lit plate.

An LBS display can be generally divided into two parts including a laser illumination module and a set of MEMS mirrors. Unlike panel-based display systems, the form factor of a LBS display remains unchanged when increasing the pixel density and FoV [59],

since there is no real object plane and pixel information is encoded in the angular domain. Conventionally, in the laser module, the separated RGB laser beams are collimated and then combined before sending it to the scanning MEMS mirror. Combiners can be a simple X-cube, or a series of mirrors or prisms with dichroic coatings allowing wavelength-selective reflection and transmission of collimated RGB laser beams, as shown in Fig. 2-8(a). A combiner system occupies the valuable space in light engine and requires precise assembly and alignment processes. A new design [60] is proposed to eliminate any additional combining optical elements by correcting the angular offset of RGB laser beams with software compensation in the time domain, as shown in Fig. 2-8(b). Two common lenses are used for collimating the RGB laser beams, and the non-coaxial beams intersect at the MEMS mirror plane with a tilt angle. The three laser diodes are shifted accordingly in the propagation direction in order to compensate for the wavelength-dependent back focal length of lenses. A widely used MEMS mirror configuration is to cascade two 1D MEMS mirrors adopting raster scanning method. The first MEMS mirror has a small diameter and is driven in resonance frequency for horizontal scan. The 1D picture is then sent to a much larger second MEMS mirror for linear scan in the vertical axis. The advantages of this design are the wider angular swing space and faster scan speed. But the drawback is larger form factor since two MEMS mirrors need to be aligned and the driving electronics is more complex. The size of the LBS light engine can be dramatically reduced by using a single 2D MEMS mirror, which can scan in both axes. But the tradeoffs are the possible crosstalk between two axes and the lower frame rate. A LBS with volume less than 1 cm^3 has been demonstrated [61].

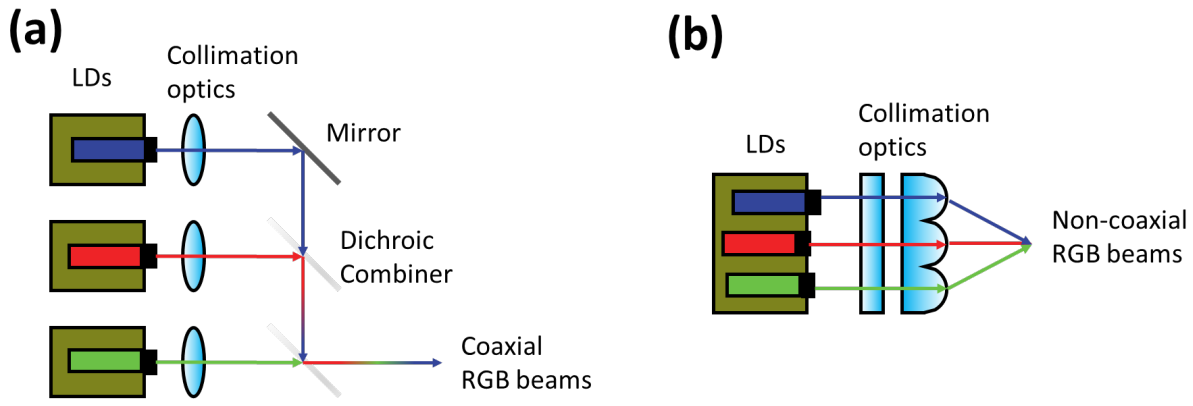

Figure 2 - 8 (a) A laser module with separate hermetically sealed RGB laser diodes, separate collimation lenes and a dichroic beam combiner. (b) RGB laser diodes are integrated in one package and share collimation optics without a beam combiner.

CHAPTER 3 LIQUID CRYSTAL BASED OPTICAL ELEMENTS

3.1 Basics of Liquid crystal

Liquid crystals [62] are mesophases between crystalline solid and isotropic liquid. The LC molecules can be elongated rod-like or disk-like. Since the LC molecules are non-spherical symmetric and they are in a mesophase, they may behave in some positional order and orientation order, to some degree. LCs in the nematic phase have no positional order but they have orientation order. A unit vector $\vec{n}$, commonly called LC director, is usually used to describe the average orientation of local LC molecules. If we add chiral dopant into a nematic host, the LC will form a helical structure. This helical structure is called cholesteric liquid crystal (CLC), a derivative of nematic LC.

The highly stable helical structures of CLC lead to a selective reflection in wavelength and circular polarization, where only the circularly polarized light with the same handedness of CLC helical structure will be strongly reflected. The handedness of the CLC helix is controlled by the handedness of the chiral dopant and the central wavelength $\bar{\lambda}$ of Bragg reflection is governed by Eq. (3-1):

$$\bar{\lambda} = \bar{n} \cdot P_{CLC} \tag{3-1}$$

where $\bar{n} = (n_e + n_o)/2$ is the average refractive index, and P_{CLC} is the pitch length. In a nematic LC mixture based on chiral dopants, the pitch is equal to Eq. (3-2)

$$P_{CLC} = \frac{1}{c \cdot HTP} \tag{3-2}$$

where c is the chiral dopant concentration and HTP is the helical twisting power of the chiral dopants. HTP is the parameter indicating the efficiency of the chiral dopants to induce a twist in a nematic LC host. The spectral bandwidth of a CLC cell is governed by Eq. (3-3):

$$\Delta\lambda = \Delta n \cdot P_{CLC} \qquad (3-3)$$

where $\Delta n = n_e - n_o$ is the birefringence of the employed LC.

3.2 Basics of diffraction grating

Gratings represent periodic modulation of refractive index. As depicted in Fig. 3-1(a), the incident light onto the grating will be diffracted into multiple orders and the diffraction angle is related to the incident angle and the horizontal periodicity by following grating equation, Eq. (3-4):

$$n_{out}\, sin\, \theta_{out} - n_{in}\, sin\, \theta_{in} = \frac{m\lambda}{\Lambda_x} \qquad (3-4)$$

where m is the order of diffraction, θ_{in} is the incident angle, θ_{out} is the diffraction angle, Λ_x is the horizontal period, and n_{in} and n_{out} is the refractive index of the input and output medium, respectively. For simplicity, we assume the input and output regions are index matched with the grating, i.e., $n_{in} = n_{out} = n_g$. Eq. (3-4) shows the inherent color dispersion of the grating. That is, even the refractive index of the grating n_g is non-dispersive, the diffraction angle still depends on the wavelength. Diffraction efficiency is defined as the power ratio of a given order to the total input light. For a thin grating, high diffraction efficiency is achievable in the blazed grating design. But for a thick grating, high diffraction efficiency is usually achieved by matching the Bragg condition. When the

input and output light k-vectors $\vec{k}_{in}$ and $\vec{k}_{out}$ form a triangular relation with the grating vector $\vec{k}_G$, depicted in Fig. 3-1(b). At Bragg condition, maximum interaction between input light and grating occurs, so the diffraction efficiency for that order is usually the highest. When the k-vectors do not perfectly match the Bragg condition due to the deviation in incident angle or wavelength, the diffraction efficiency drops; the extent of efficiency drop is related to the index modulation within the grating. The high efficiency spectral and angular bandwidth is proportional to the degree of index modulation.

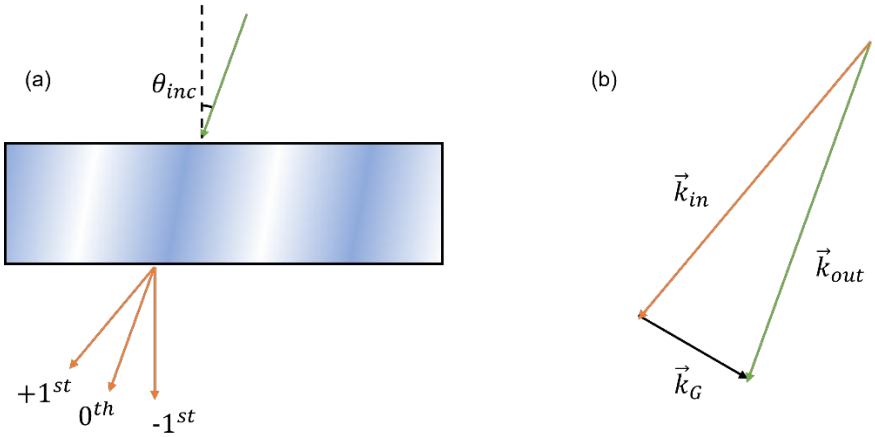

Figure 3 - 1 Basic configuration of the grating diffraction: (a) plot of the input light and multiple diffraction orders, and (b) sketch of Bragg condition.

To classify the grating quantitatively, two dimensionless parameters $Q = 2\pi\lambda d/\bar{n}\Lambda_x^2$ [63] and $\rho = 2\lambda^2/\bar{n}\Delta n_l\Lambda_x^2$ [64] are frequently used to identify the grating regimes, where λ is the wavelength, d is the grating thickness, $\bar{n}$ is the average refractive index, Δn_l is the modulation of the refractive index in the coupled wave theory, and Λ_x is the grating horizontal period. It is shown that when $Q\ or\ \rho \leq 1$, the gratings are classified as Raman-Nath gratings or thin gratings, and when $Q\ or\ \rho \gg 1$, the gratings fall into Bragg regime, or are referred to be thick.

3.3 LC gratings

Liquid crystal based optical elements (LCOEs) are generally referred to as planar diffractive devices formed by spatially controlling the LC director orientation. These devices include gratings, lenses and manifest unique features including high diffraction efficiency (~100%), compact form factor (1~4μm), relatively broad angular and spectral bandwidth, polarization sensitivity, simple fabrication process, and low manufacture cost. The peculiar polarization sensitivity provides an extra degree of freedom to utilize and control the light. Any LCOE can be viewed as a grating locally, so the discussion on LC gratings can be extended to other LCOEs. LC gratings are also called polarization gratings (PGs). The diffraction in PGs is based on the spatially oriented LC directors, so the index modulation is equal to the LC birefringence $\delta n = \Delta n = n_e - n_o$. Thanks to the matured LCD industry, nowadays the LC birefringence can cover a wide range $(0.05 \sim 0.4)$, which gives us great tunability in the angular and spectral bandwidth.

According to the diffraction direction, PGs can be classified into two types: reflective polarization grating (r-PG) and transmissive polarization grating (t-PG). They are fabricated by photoalignment polarization holography (PAPH). In PAPH, a thin photoalignment layer (PAL), usually consists of azo compound, is spin-coated onto a glass substrate. The exposed polarized light then induces optical anisotropy in the PAL, which is formed by photoisomerization. The azo compound molecules repeatedly go through trans-cis photoisomerization cycles and are reoriented perpendicular to the long axis of general elliptical polarization state, where the absorption of light is minimal. Therefore, linear polarization state has the best reorienting capacity. The LC material used in PAPH could be a fluidic LC or a reactive mesogen. The former is usually used in

fabricating active devices since it keeps the electrical tunability and the latter is a polymerizable LC with reactive end groups, which is commonly used in passive devices. The reactive mesogen is usually mixed with photo-initiator and dissolved in an organic solvent. To fabricate passive devices, the LC mixture is spin-coated over the PAL after the recording process and illuminated by ultraviolet (UV) light. The reactive mesogen then form the polymer network with high thermal and chemical stabilities.

The basic principle of PAPH is shown in Fig. 3-2.

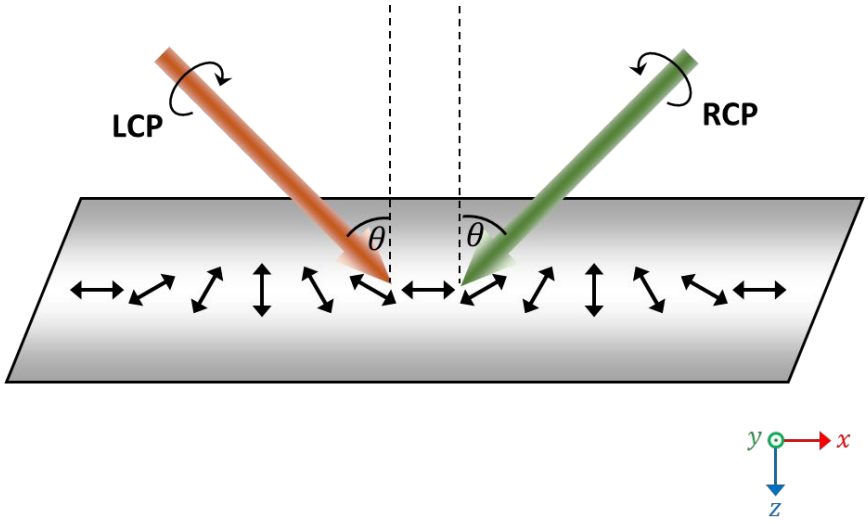

Figure 3 - 2 Schematics of PAPH. Interference of LCP and RCP light to produce a sinusoidal linearly polarized pattern.

When two circularly polarized (CP) beams with opposite handedness interfere, the electric field on the recording plane exhibits a sinusoidal linear polarization pattern along the x-axis, which can be approximated by the following Eq. (3-5):

$$\begin{bmatrix}1\\ i\end{bmatrix} e^{-ik_0 \sin\theta \cdot x} + \begin{bmatrix}1\\ -i\end{bmatrix} e^{+ik_0 \sin\theta \cdot x} = 2\begin{bmatrix}cos(k_0 \sin\theta \cdot x)\\ sin(k_0 \sin\theta \cdot x)\end{bmatrix} \qquad (3-5)$$

where k_0 is the wavenumber, and θ is the incident angle. The photoalignment material, which tends to align perpendicular to near linear polarization orientation, records the

pattern. Due to self-assembly, the bulk LC molecules follow the in-plane crystal axis defined by PAL. For t-PGs, when the period is large (>2μm), which belongs to the Raman-Nath regime, they are commonly referred to Pancharatnam-Berry phase deflector (PBD) since its operation mechanism is based on the geometric phase of patterned half-wave plate. The optical properties of PBD are well illustrated by the simple Jones matrix. The local Jones matrix of a PBD can be written as Eq. (3-6):

$$T(x) = R\big(\varphi(x)\big)\begin{bmatrix} e^{-\frac{i\Gamma}{2}} & 0 \\ 0 & e^{\frac{i\Gamma}{2}} \end{bmatrix} R\big(-\varphi(x)\big) \tag{3-6}$$

where $\Gamma = 2\pi\Delta nd/\lambda$ is the LC phase retardation, $R = \begin{bmatrix} \cos\theta & -\sin\theta \\ \sin\theta & \cos\theta \end{bmatrix}$ is the rotation matrix, and $\varphi(x) = \pi x/\Lambda_x = k_0 \sin\theta \cdot x$ is the LC azimuthal angle. It can be seen that $T(x)$ is a periodic function with periodicity $\Lambda_x = \lambda_0/(2\sin\theta)$. As shown in Eq. (3-7), Eq. (3-8), Eq. (3-9) and Eq. (3-10), by performing Fourier series decomposition, only three orders are found in $T(x)$:

$$T_m = \frac{1}{\Lambda_x}\int_0^{\Lambda_x} T(x) e^{-\frac{im2\pi x}{\Lambda_x}} dx \tag{3-7}$$

$$T_0 = cos\left(\frac{\Gamma}{2}\right)\begin{bmatrix} 1 & 0 \\ 0 & 1 \end{bmatrix} \tag{3-8}$$

$$T_1 = \frac{1}{2} sin\left(\frac{\Gamma}{2}\right)\begin{bmatrix} -i & -1 \\ -1 & i \end{bmatrix} \tag{3-9}$$

$$T_{-1} = \frac{1}{2} sin\left(\frac{\Gamma}{2}\right)\begin{bmatrix} -i & 1 \\ 1 & i \end{bmatrix} \tag{3-10}$$

Thus, diffraction efficiency can be calculated as $D_0 = \cos^2(\Gamma/2)$, $D_{+1} = 1/2\sin^2(\Gamma/2)(1 - S_3')$ and $D_{-1} = 1/2\sin^2(\Gamma/2)(1 + S_3')$, where S_3' is the normalized Stokes parameter S_3. It

should be noticed that the optical period Λ_x is half of the horizontal LC pitch, which means LC molecules only rotate π in one grating period Λ_x. When the half-wave phase retardation condition is satisfied, the transmitted polarization state can be calculated as Eq. (3-11).

$$T_{HWP}\begin{bmatrix}1\\ \pm i\end{bmatrix} \sim \begin{bmatrix}cos(2\pi x/\Lambda_x) & sin(2\pi x/\Lambda_x)\\ sin(2\pi x/\Lambda_x) & -cos(2\pi x/\Lambda_x)\end{bmatrix}\begin{bmatrix}1\\ \pm i\end{bmatrix} = \begin{bmatrix}1\\ \mp i\end{bmatrix} e^{\pm\frac{i2\pi x}{\Lambda_x}} \qquad (3-11)$$

One can see that the handedness of incident CP light is flipped, and RCP and LCP lights are directed into ± 1 diffraction orders and the diffraction efficiency is 100% for a pure CP light, in theory, as shown in Fig. 3-3. By introducing a small quantity of chiral dopants into the LC mixture and employing a multi-twist structure, the angular and spectral response of the PBD can be expanded. For accurate structure optimization of a broadband PBD, the Jones matrix or the transfer matrix method can be utilized, providing swift calculation speeds, especially for pitches greater than 2 μm. In cases of smaller pitches, more precise simulation tools such as finite-difference time-domain (FDTD) or Rigorous Coupled-Wave Analysis (RCWA) methods are necessary.

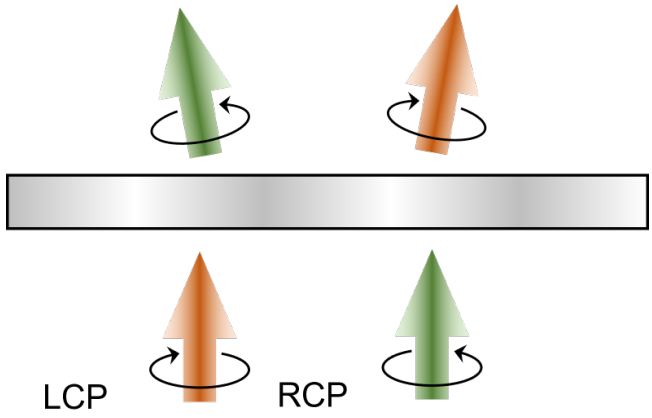

Figure 3 - 3 A PBD based on nematic LC. The optical response for RCP and LCP is symmetric.

When the period gets smaller, the PGs gradually fall into the Bragg regime and usually only show high efficiency in one diffraction order. As the paraxial approximations fails, one needs more accurate numerical methods to simulate the optical response.

For the r-PG, it is necessary to incorporate chiral dopants into the LC mixture, and the required concentration significantly exceeds that used for t-PG. The diffraction direction is dictated by the horizontal pitch, while the diffraction efficiency can be modulated by adjusting both the concentration of the CLC mixture and the thickness of the film or cell. As a general guideline, the thickness should span approximately 10 CLC pitches to attain an efficiency exceeding 90%. Such fine-tuning is critical to fulfill the Bragg condition.

3.4 Simulation methods

Recently, RCWA is found to be an efficient and accurate approach to investigate PGs [65], since the dielectric tensor is smooth in PGs and only one or two dominant diffraction orders exist. In RCWA, the electric and magnetic fields in the PGs are expressed in Fourier expansions to order M, as shown in Eq. (3-12) and Eq. (3-13), according to the grating period:

$$\begin{aligned}\vec{E}_g(x,z) &= e^{-j(k_{x0}x+k_{y0}y)}\sum_m \vec{S}_m(z)e^{jm(K_xx+K_zz)} \\ &= \sum_m \vec{S}_m(z)e^{-j(k_{x,m}x+k_{y0}y+k_{z,m}z)}\end{aligned} \qquad (3-12)$$

$$\begin{aligned}\vec{H}_g(x,z) &= e^{-j(k_{x0}x+k_{y0}y)}\sum_m \vec{U}_m(z)e^{jm(K_xx+K_zz)} \\ &= \sum_m \vec{U}_m(z)e^{-j(k_{x,m}x+k_{y0}y+k_{z,m}z)}\end{aligned} \qquad (3-13)$$

where k_{x0}, k_{y0} are the horizontal wavevector component of the incident light and K_x, K_z are the grating vector components in x direction and z direction, respectively.

The formulation of RCWA starts from the two normalized curl Eq. (3-14) and Eq. (3-15) from Maxwell's equations in the frequency domain:

$$\nabla \times \vec{E} = k_0 \vec{H} \tag{3-14}$$

$$\nabla \times \vec{H} = k_0 \varepsilon_r \vec{E} \tag{3-15}$$

where ε_r is the permittivity tensor of the PGs, which is a symmetric tensor Eq. (3-16):

$$\varepsilon_r = \begin{bmatrix} \varepsilon_{xx} & \varepsilon_{xy} & \varepsilon_{xz} \\ & \varepsilon_{yy} & \varepsilon_{yz} \\ & & \varepsilon_{zz} \end{bmatrix} = R \begin{bmatrix} n_o^2 & & \\ & n_o^2 & \\ & & n_e^2 \end{bmatrix} R^{-1} \tag{3-16}$$

where R is the rotation matrix determining the LC directors' orientation in the PGs, and n_e and n_o is the LC extraordinary and ordinary refractive index, respectively.

Field components in the z direction is eliminated and arranged as Eq. (3-17):

$$\frac{\partial}{\partial u} \begin{bmatrix} S_x \\ S_y \\ U_x \\ U_y \end{bmatrix} = M \begin{bmatrix} S_x \\ S_y \\ U_x \\ U_y \end{bmatrix} \tag{3-17}$$

where $u = k_0 z$, S_x, S_y, U_x, U_ycontain the tangential fields in each diffraction order.

And this equation can be easily solved by diagonalizing matrix M Eq. (3-18):

$$M = WQW^{-1} \tag{3-18}$$

Thus, we can correlate the input and output fields by matching the tangential fields at each interface, and the transmission and reflection diffraction efficiencies in each diffraction order can be calculated. If the PGs' structures contain several layers of different LC director distribution, then scattering matrix or enhanced transmittance matrix methods can be applied.

Since we are interested in the output polarization states in each diffraction order, especially if the CP states are well maintained, Stokes parameters are a good tool to monitor the polarization states. By extracting the output electric field $E_{\parallel}$ and $E_{\perp}$ components in two orthogonal directions, the degree of CP states can be calculated by normalizing the Stokes parameter [66] S_3' Eq. (3-19):

$$S_3' = -\frac{2\boldsymbol{Im}(E_{\parallel}E_{\perp}^*)}{E_{\parallel}^2 + E_{\perp}^2} \qquad (3-19)$$

where **Im** indicates the imaginary parts.

Building on our thorough investigation of LC devices' optical properties and simulation techniques, we are well-prepared to convert these theoretical insights into practical innovations. In Chapter 5, we harness the polarization selectivity of LC lenses to develop compact foveated AR displays powered by a single light engine. Moving forward, Chapter 6 describes our utilization of reflective polarization gratings to approach the full-color FoV limit within a single-layer waveguide AR display. These chapters demonstrate the direct application of our foundational research to advance the frontier of AR display technology.

CHAPTER 4 LOW-DIFFRACTION TRANSPARENT μLED DISPLAYS

The content of this chapter was previously published in [67].

4.1 Background

Transparent display is a promising technology with potential applications in smart windows, automotive windshield displays, Under-Display Cameras, Under-Display Sensors as well as augmented reality displays for showcase [2,3], to name a few. The emerging μLED technology [68–70] is a promising solution for transparent displays because of its high brightness and large aperture ratio due to the small chip size and inorganic emissive nature [71]. Sony has successfully developed a tiled 16K μLED screen with 99% aperture ratio [72], which shows an outstanding ACR, although the pixel per inch is only about 20. For AR automotive applications, clear and vivid images from the display itself (foreground) and the scene after display (background) are both desired. Also, high illuminance and high ACR are necessary for outdoor scenarios [36]. Conventional projection type HUDs adopt a more complex system design including a light engine, reflective mirrors, and an optical combiner [49,73]. With a transparent display on the windshield, a much simpler system design can be realized for a monoscopic AR display [74]. Moreover, due to inherent transparency and self-illumination, higher optical efficiency, wider color gamut, larger eyebox and FoV can be expected in a transparent HUD. Compared to μOLED [75,76], μLED does not have the tradeoff between high illuminance and lifetime, which suggests that the μLED chip size can be smaller for achieving a higher transparency. Yet, in a transparent μLED display, the see-through images are often blurred caused by light diffraction after passing through the periodic

pixel structures [16]. Our study shows that the image quality deteriorates more if the objects are far away from the display panel, which is a common situation while driving.

For smartphone applications, manufacturers are pursuing bezel-less, full-screen designs with high pixel density to enhance the interaction between users and devices. Under-display camera is a new trend to achieve a sleek industrial design but mounting the display in front of a camera will also cause severe image degradation. Deep learning related algorithms are adopted to restore the blurred images by modelling different optical effects caused by the display, camera lens and human vision system, but real-time algorithms are hard to be applied in preview and video mode currently [77]. Thus, it is of great importance to suppress the diffraction effect from the optics viewpoint, especially for high pixel density devices where a high aperture ratio is difficult to achieve.

Transparent display is essentially a binary aperture function from the viewpoint of diffraction theorem, where the transmittance is 1 in open regions and 0 in opaque regions. Tsai et al. [78] studied the diffraction widths with a Gaussian beam passing through apertures with different pixel structures and assumed that a narrower diffraction width could mitigate the diffraction effect. This assumption does not take human factors into account so that the result might lead to some uncertainty due to the finite aperture size (in the order of millimeters). Qin et al. [79] proposed to simulate diffracted see-through images and evaluate the pixel structures with subjective image quality score. To our knowledge, no simple, reference-image independent and physically intuitive evaluation methodology is proposed for the diffraction effect of transparent displays with human factors considered. In this paper, we first build our quantitative evaluation method for the diffraction effect perceived by human eyes and then analyze the magnitude of diffraction

in a conventional pixel structure with various object distances, resolutions, and aperture ratios. A pixel structure optimization method is introduced to minimize the diffraction effect for transparent displays with a small aperture ratio.

4.2 Theory

The point spread function (PSF) is the response of an incoherent imaging system to an input point source, while the blurred images can be obtained by convolution of the objects and the PSF. Thus, by studying the PSF of an imaging system including a transparent display and a human eye, one can investigate the diffraction effect of pixel structures. Fig. 4-1 shows the schematics of the imaging system, where the light from background objects propagates in free space for d_1 before passing through the transparent display. A human eye is modeled as a positive lens with focal length f, positioned at d_2 after the transparent display, U_1 is a virtual plane immediately in front of the lens to assist in the derivation, and the imaging plane (U_2) is located on the retina.

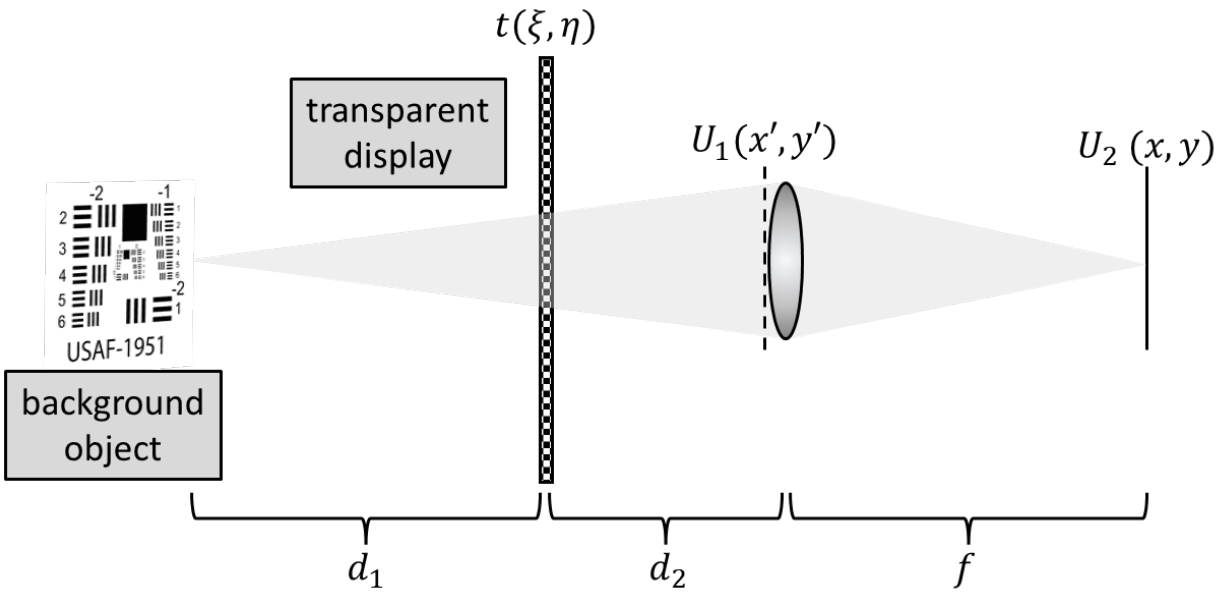

Figure 4 - 1 Schematics of the imaging system.

The derivation of the monochromatic PSF with a finite object distance d_1 has been reported in [79] and the system PSF on the retina can be expressed as follows:

$$h(x,y) \propto \left| \mathcal{F}\{t(\xi,\eta)\}|_{f_x=\frac{x}{\lambda M f}, f_y=\frac{y}{\lambda M f}} \right|^2, \qquad (4-1)$$

where f_x and f_y is the spatial frequency in x and y direction, respectively, λ is the wavelength, and script letter $\mathcal{F}$ is the symbol for Fourier Transform (FT). In Eq. (4-1), the finite pupil size of human eye is ignored since this study focuses on the diffraction from display panel. In this imaging system, the PSF $h(x,y)$ is the modulus square of FT of the aperture distribution $t(\xi,\eta)$. The human eye acts as a lens and the retina as the receiver plane. The optical power of human eye can be dynamically adjusted to satisfy the object-image relation, approximated by the Gaussian optics [38] in Eq. (4-2), following the convention in a Cartesian coordinate system,

$$\frac{1}{s_o} + \frac{1}{s_i} = \frac{1}{f}, \qquad (4-2)$$

where s_i and s_o are the image and object distances, and f is the focal length of the eye. In human eyes, the image distance can be regarded as the distance between pupil and retina, which is ~17 mm.

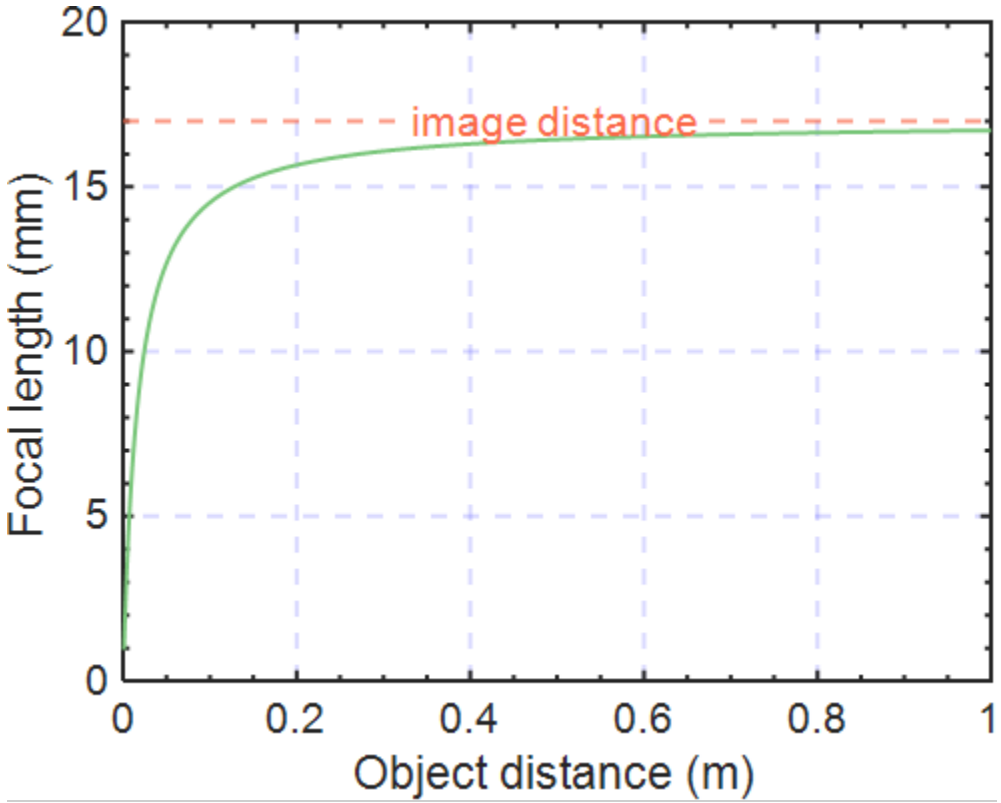

Figure 4 - 2 Focal length f of the eye as a function of object distance.

In Fig. 4-2, the focal length of the eye is plotted as a function of the object distance. When the object distance is 30 cm, the focal length is about 16 mm, which suggests that treating the focal plane as the imaging plane is a good approximation for any object distance farther than 30 cm. We choose focal length f=17 mm in the following simulations.

Parameter $M=d_1/(d_1+d_2)$ is a metric for relative object distance from the transparent display and $M=1$ when the object is at infinity. The transparent display is regarded as a 2D aperture function $t(\xi,\eta)$, where amplitude transmittance is defined as either 0 (opaque) or 1 (transparent) at each point. The opaque area includes the emitting unit and the circuits, and the rest area is transparent. In Fourier optics, the display panel with periodic pixel arrangement can be modeled as a 2D grating as it redistributes the incident light into various diffraction orders. Therefore, following the convention in [79], the aperture

function $t(\xi,\eta)$ can be modeled by convolution between a unit cell function $t_0(\xi,\eta)$ and a comb function and constrained by finite boundaries represented by a rectangular function, as shown in Eq. (4-3),

$$t(\xi,\eta) = \left[t_0(\xi,\eta) \otimes \mathrm{comb}\left(\xi/L_{x_0}, \eta/L_{y_0}\right)\right] \times \mathrm{rect}(\xi/L_x)\mathrm{rect}\left(\eta/L_y\right), \qquad (4-3)$$

where L_{x0} and L_{y0} are the size of the unit cell, and L_x and L_y are the actual size of the display panel. Its FT can be expressed as Eq. (4-4):

$$h(x,y) \propto \left|\left[h_0\left(f_x,f_y\right) \times \mathrm{comb}\left(L_{x_0}f_x, L_{y_0}f_y\right)\right] \otimes \mathrm{sinc}(L_x f_x)\mathrm{sinc}\left(L_y f_y\right)\right|^2_{f_x=\frac{x}{\lambda M f}, f_y=\frac{y}{\lambda M f}}, \quad (4-4)$$

where $h_0(f_x,f_y)$ is the FT of $t_0(\xi,\eta)$.

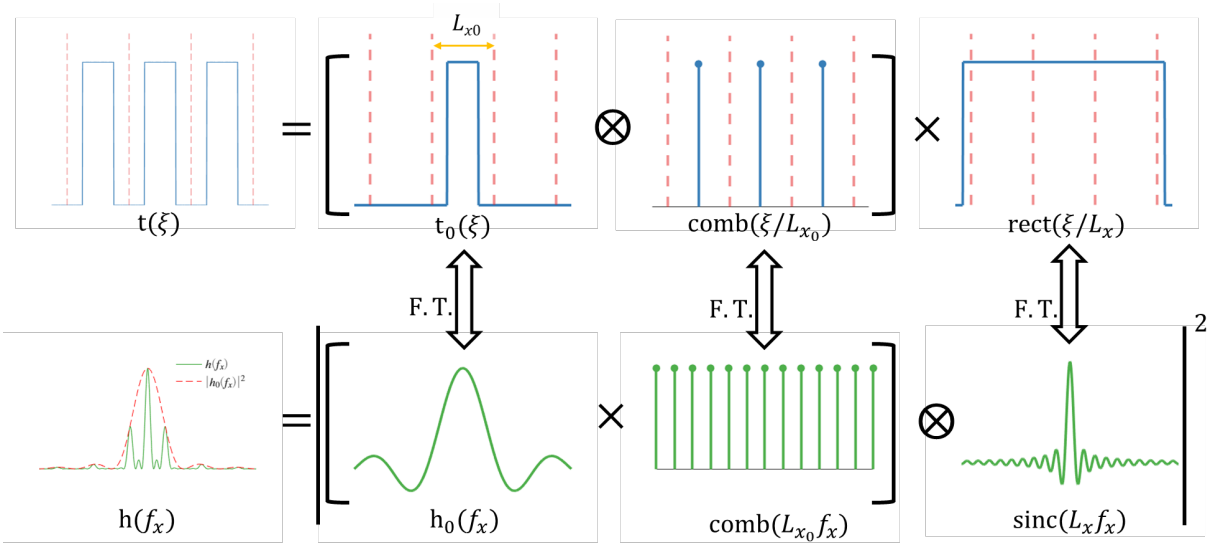

Figure 4 - 3 A visual representation of PSF calculation in an imaging system including a transparent display. For simplicity, 1D derivation is shown here but it is easy to extend to two dimensions.

In Fig. 4-3, an intuitive demonstration of how to efficiently calculate the system PSF is illustrated, where the FT of unit cell function $t_0(\xi,\eta)$ can be solved first and then PSF $h(x,y)$ is analytically obtained. Due to the complex aperture structure, sometimes the analytical derivation is not possible and numerical simulation is performed with the aid of fast Fourier

Transform (FFT) algorithm. In this way, tremendous computational load is greatly relieved, while accurate PSF is still guaranteed. If the physical size of the unit cell is set to be L_{0x}×L_{0y} and sampling points are N_x×N_y, then the physical size on the receiver plane should be $N_xM\lambda f/L_{x0}$ × $N_yM\lambda f/L_{y0}$. The comb function in PSF expression indicates the spacing between diffraction orders on the retina is $M\lambda f/L_{x0}$ and $M\lambda f/L_{y0}$ in x and y direction and the *sinc* function means that each diffraction order has a finite diffraction width $M\lambda f/L_x$ and $M\lambda f/L_y$. The angular resolution of the human eye is 1 arcminute and its corresponding length on the retina is 5μm. Since the energy mainly concentrates in the zeroth diffraction order, located in the center of imaging plane, and gradually decreases in the higher orders, it is reasonable to assume that only diffraction orders that are 5-μm away from the zeroth order can be distinguished by the eye. Those closer diffraction orders are blended with zeroth order, indistinguishable to human eye. Therefore, a relative diffraction intensity, defined as maximum diffraction intensity outside the 5-μm region to the zeroth order intensity, is used to quantitatively characterize the diffraction effect of transparent display to human eye. The diffraction width of the *sinc* function is about tens of nanometers or less for a display panel with 103~104 pixels in each dimension, which is relatively small compared with human eye resolution and thus can be ignored in the PSF calculation. That means the system PSF can be simplified as a comb function modulated by FT of unit cell function $t_0(\xi,\eta)$.

4.3 Conventional pixel structures

In conventional pixel structures, the positions of the opaque region in each pixel are the same. The impact of object distance, panel resolution, and pixel aperture ratio on the diffraction effect to human eye is analyzed by our model. Without losing generality, we

assume the pixel geometry is square with side length *p* and the opaque region geometry is also square, located in the center of each pixel, since the diffraction effect is found to be irrelevant to pixel/opaque geometry [79]. Unlike the definition in [68], here the aperture ratio α represents the area of transparent region to that of the pixel. The side length of opaque region *b* is determined by the aperture ratio *α*, proportional to the square root of *1-α*. Noticing that the spacing between diffraction orders is proportional to the parameter M. If M is small, the PSF is scaled down and most energy is within 5μm from the zeroth diffraction order so that the diffraction effect is negligible. Hence, the diffraction effect is most obvious when the object is at infinity (M = 1) and the following analyses are taken under this extreme scenario.

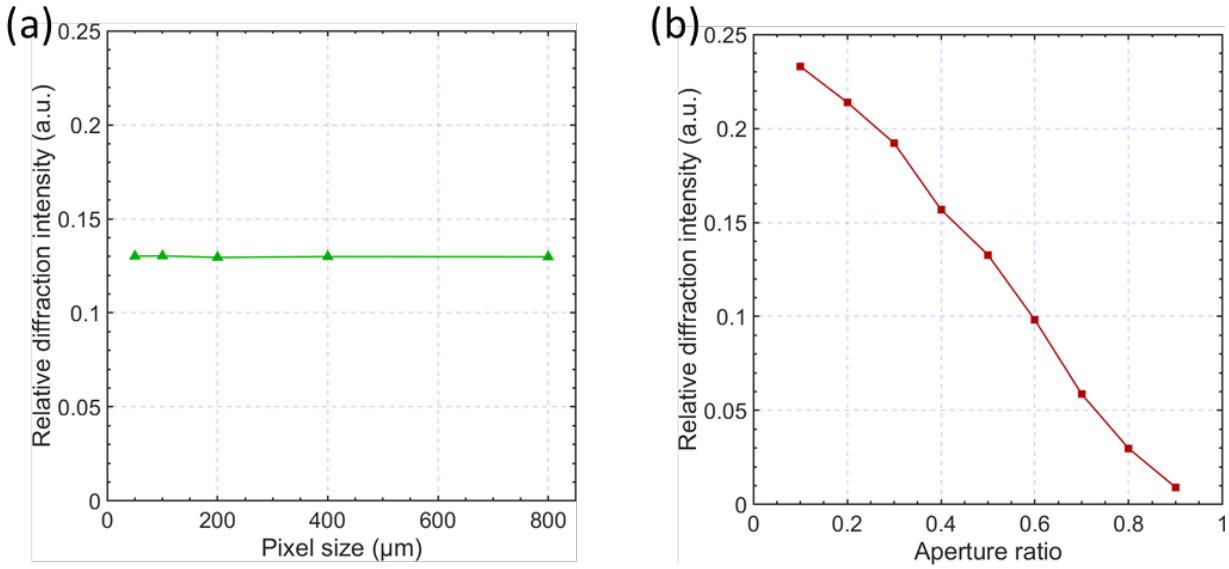

Figure 4 - 4 (a) At aperture ratio α=50%, the normalized diffraction intensity is invariant to the pixel size p=50~800μm. (b) With pixel size p=400μm, the normalized diffraction intensity decreases as aperture ratio α increases from 10% to 90%.

The panel resolution is determined by the pixel size. For common display devices, the pixel size ranges from tens of microns (smartphones) to hundreds of microns (TVs). In Fig. 4-4(a), the aperture ratio is set at α=50% and the normalized diffraction intensity is

invariant to the pixel size. This result seems counter-intuitive at the first glance because diffraction effect is generally more obvious with finer structure, but it coincides with the conclusion in [78], by evaluating the subjective score of see-through images. From Eq. (4-3), the pixel size only impacts the coordinate transformation in the PSF calculation and the diffraction order spacing is inversely proportional to the pixel size. Even with an unrealistically large pixel size p=1000μm, the order spacing is 9.35μm at a green light (λ=550nm). Since the diffraction order spacings are larger than human eye's angular resolution, the same diffraction intensity is observed by human.

Another important impact factor is the aperture ratio. In Fig. 4-4(b), the pixel sizes are set to be 400μm, and the normalized diffraction intensity decreases as the aperture ratio increases from 10% to 90%. According to the similarity theorem of FT, the open region is stretched at a higher aperture ratio and its PSF is squeezed, leading to a lower diffraction intensity. It seems that boosting the aperture ratio of pixels is the only way to suppress diffraction effect in the conventional pixel structures. The aperture ratio is directly related to the chip size of the employed LED. However, even with μLED technology, it is still difficult to achieve a large aperture ratio while maintaining high resolution with current fabrication technologies. It would be of practical interest for smartphone applications if the diffraction effect could be reduced even at a small aperture ratio.

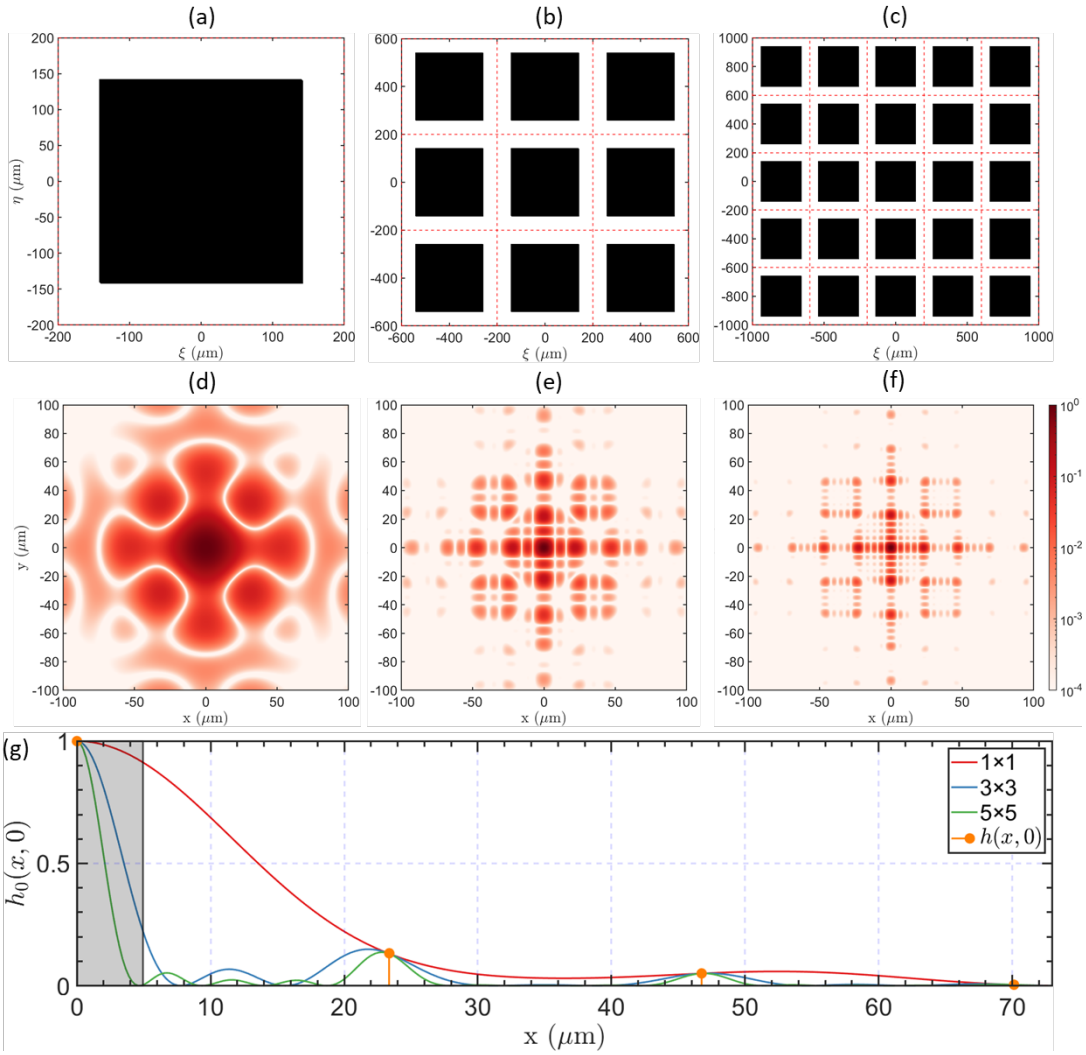

Figure 4 - 5 (a-c) With pixel size p=400μm and aperture ratio α=50%, unit cell functions *t₀(ξ,η)* with 1×1, 3×3, 5×5 pixels in one unit cell for conventional pixel structures. (d-f) FTs of unit cell functions in (a-c). (g) The horizontal cross-section *h₀(x,y)* excerpted from (d-f).

4.4. Optimized pixel structures

In Fig. 4-3, the size of unit cell function $t_0(\xi,\eta)$ is the same as the pixel size, but in fact the unit cell could include more pixels and final PSF will be the same for conventional pixel structures. With p=400μm and α=50%, Figs. 4-5(a-c) show the $t_0(\xi,\eta)$ with 1×1, 3×3, 5×5 pixels in one unit cell, respectively, and their FT $h_0(x,y)$ in Figs. 4-5(d-c) look quite different. Fig. 4-5(f) shows their horizontal cross section $h_0(x,0)$ and they all converge to the same PSF h(x,0) after multiplying by comb functions with corresponding diffraction

order spacing. After all, in conventional pixel structures, the choice of unit cell only affects how we represent the same aperture function $t(\xi,\eta)$ mathematically and their PSFs remain the same physically. Nevertheless, it is enlightening that optimizing the pixel structures within a unit cell $t_0(\xi,\eta)$ containing several pixels could possibly decrease the diffraction intensity. Here, the coordinates of the opaque regions in each pixel are the optimization variables, and the diffraction intensity is the objective functions. The vertical coordinates in each row and horizontal coordinates in each column should stay the same for the ease of circuit layout and fabrication. This restriction greatly reduces the optimization variables from $2n^2$ to 2n for a unit size with n×n pixels.

In the global optimization, the unit cell sizes are set by pixel number in one dimension n=1~10 and the aperture ratios are set at α= 30%, 50% and 70%. The optimized diffraction efficiency at each case is plotted in Fig. 4-6. As the pixel number *n* increases, the diffraction efficiency decreases and gradually converges to a stable value for each aperture ratio. Before optimization, the diffraction intensity for each aperture ratio is 0.19, 0.13, and 0.06, respectively, and it drops to 0.15, 0.05, and 0.01 after optimization, where the normalized diffraction intensity drop is 21%, 62% and 83%. When pixel number *n*=1, the diffraction intensities are the same as those in an unoptimized structure due to periodicity. The diffraction intensity of an optimized pixel structure with α=50% is even lower than that of an unoptimized α=70% structure. By optimizing pixel structures in unit cells with n=2, the diffraction effect is greatly mitigated, and the normalized diffraction drops are 21%, 42% and 58% at each aperture ratio. One of the optimized cell unit pixel structures $t_0(\xi,\eta)$ for n=3 and α=50% is shown in Fig. 4-7(a) and its FT $h_0(x,y)$ and horizontal cross section $h_0(x,0)$ is plotted in Figs. 4-7(b)(c). Compared to the unoptimized

structure, the energy distribution in the optimized pixel structure avoids its peaks to be coincided with the position of diffraction orders, leading to an effectively lower diffraction intensity. This result can also be extended to smaller pixels if the relative coordinates of the opaque region in each pixel are considered as the optimization variables.

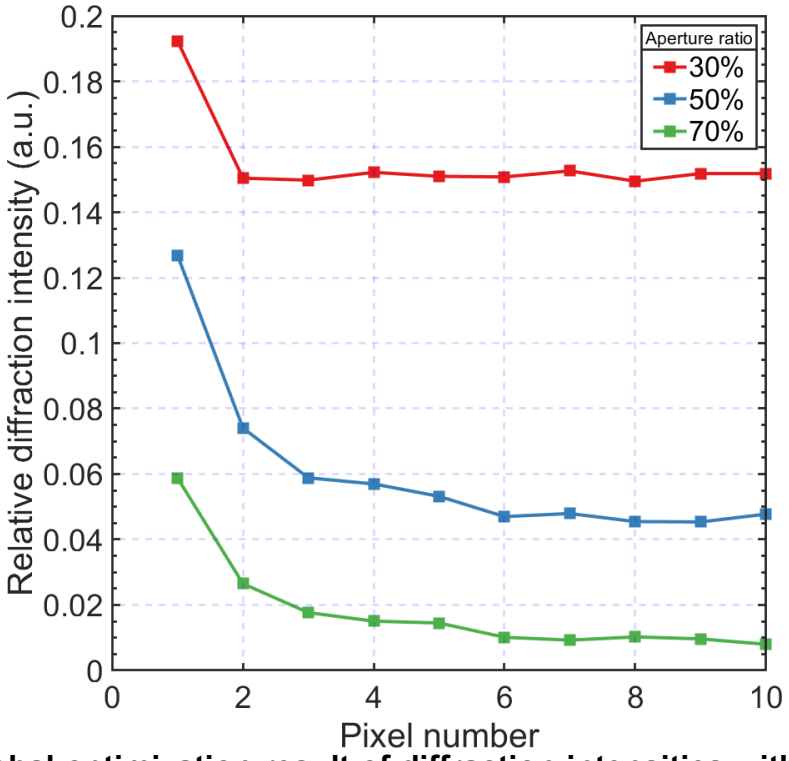

Figure 4 - 6 Global optimization result of diffraction intensities with unit cell sizes n=1~10 and aperture ratios α= 30%, 50% and 70%.

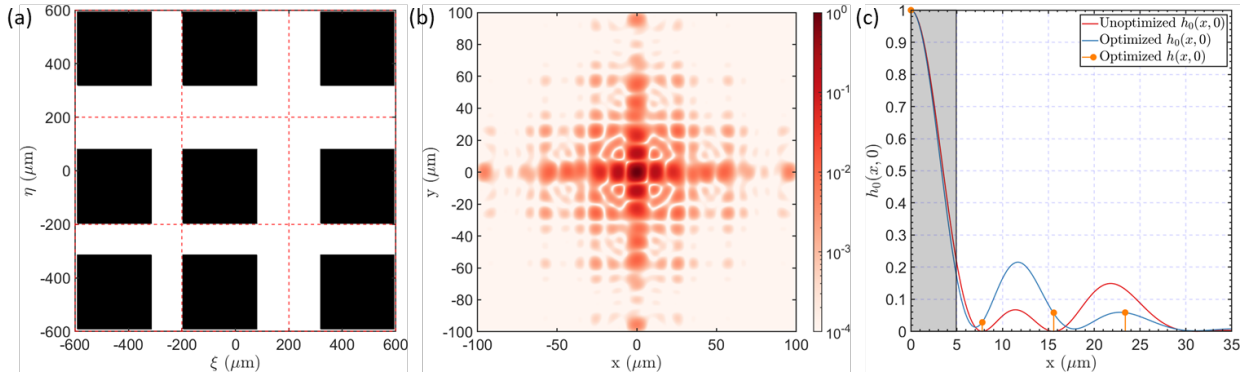

Figure 4 - 7 (a) An optimized pixel structure within a unit cell with 3×3-pixel size and aperture ratio α=50%. (b) FT of the optimized structure. (c) Horizontal cross section *h₀(x,0)* of the optimized and unoptimized structures and PSF *h(x,0)* of the optimized structure.

With the aid of PSF, the diffracted images of background objects could be obtained by convolution, assuming the display panel is viewed on-axis. It should be noticed that the PSF is wavelength dependent, thus monochromatic PSFs for each individual wavelength are essential for an RGB full-color object. For simplicity, the background objects are treated as a gray-level 2D image with a uniform reflective spectrum illuminated by a D65 light source. Before implementing the convolution, the gray-level image should be resized to maintain the same physical length at each wavelength. After the convolution, the image should be interpolated again to have the same sampling points. As in the hyperspectral imaging, the data on the receiver plane after the convolution is a stacked 2D intensity, where each pixel has its own spectrum distribution. For visualization, the spectrum information is converted to XYZ tristimulus value first, as in Eq. (4-5), Eq. (4-6) and Eq. (4-7):

$$X = k \sum_{\lambda=380\text{nm}}^{\lambda=780\text{nm}} E(\lambda)x(\lambda)P(\lambda), \qquad (4-5)$$

$$Y = k \sum_{\lambda=380\text{nm}}^{\lambda=780\text{nm}} E(\lambda)y(\lambda)P(\lambda), \qquad (4-6)$$

$$Z = k \sum_{\lambda=380\text{nm}}^{\lambda=780\text{nm}} E(\lambda)z(\lambda)P(\lambda), \qquad (4-6)$$

where E(λ) is the illumination source, P(λ) is the intensity distribution, x(λ), y(λ), and z(λ) are the CIE 1931 2-degree color-matching functions and *k* is a normalization factor. For RGB values, we choose sRGB system to perform the conversion, using the transformation matrix shown in Eq. (4-7):

$$T_{XYZ\to RGB} = \begin{bmatrix} 3.2404542 & -1.5371385 & -0.4985314 \\ -0.9692660 & 1.8760108 & 0.0415560 \\ 0.0556434 & -0.2040259 & 1.0572252 \end{bmatrix}, \qquad (4-7)$$

And a gamma correction Eq. (4-8) is performed for the computer display:

$$V = \begin{cases} 12.92v & \text{if } v \le 0.0031308 \\ 1.055v^{\frac{1}{2.4}} - 0.055 & \text{otherwise} \end{cases}, \qquad (4-8)$$

where v is the linear sRGB value and V is the nonlinear sRGB value. The XYZ values and RGB values in the calculation are forced to be in the range within 0-1, by simple clipping method where the values above 1 are suppressed to 1 and those below 0 are replaced by 0. If the values greatly exceed 1, perhaps a scaling method is preferable. The accuracy of this method has been experimentally verified in [79]. To intuitively illustrate the diffraction-suppression effect of our optimized pixel structures, three letters 'UCF' are used as background object, shown in Fig. 4-8(a). We assume d=25cm and the object size is 50mm×38mm, located 1-m away from the observer. Image blur effect with unoptimized structure is displayed in Fig. 4-8(b).

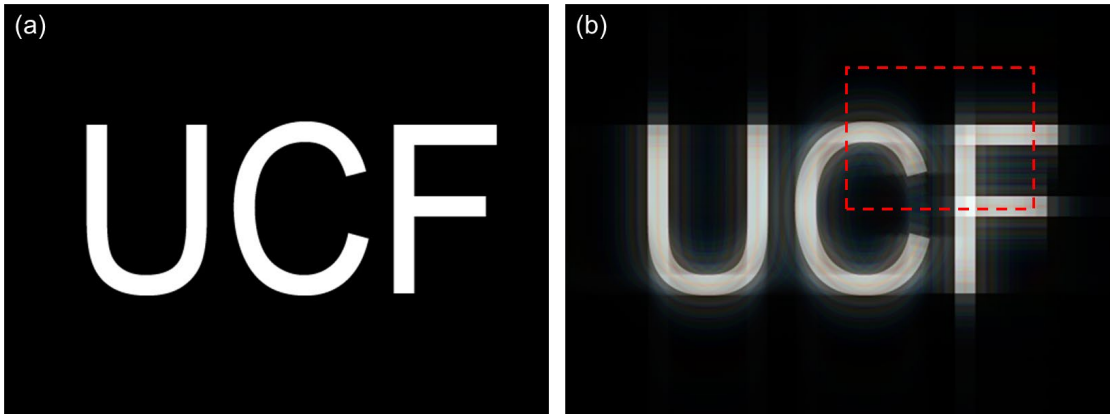

Figure 4 - 8 (a) Test background object. (b) Diffracted image with an unoptimized pixel structure at 30% aperture ratio.

Fig. 4-9 shows the improved image quality with our optimized pixel structures. The diffraction is greatly suppressed with a 2×2-pixel unit cell, comparing Fig. 4-9(d) with Fig. 4-9(e).

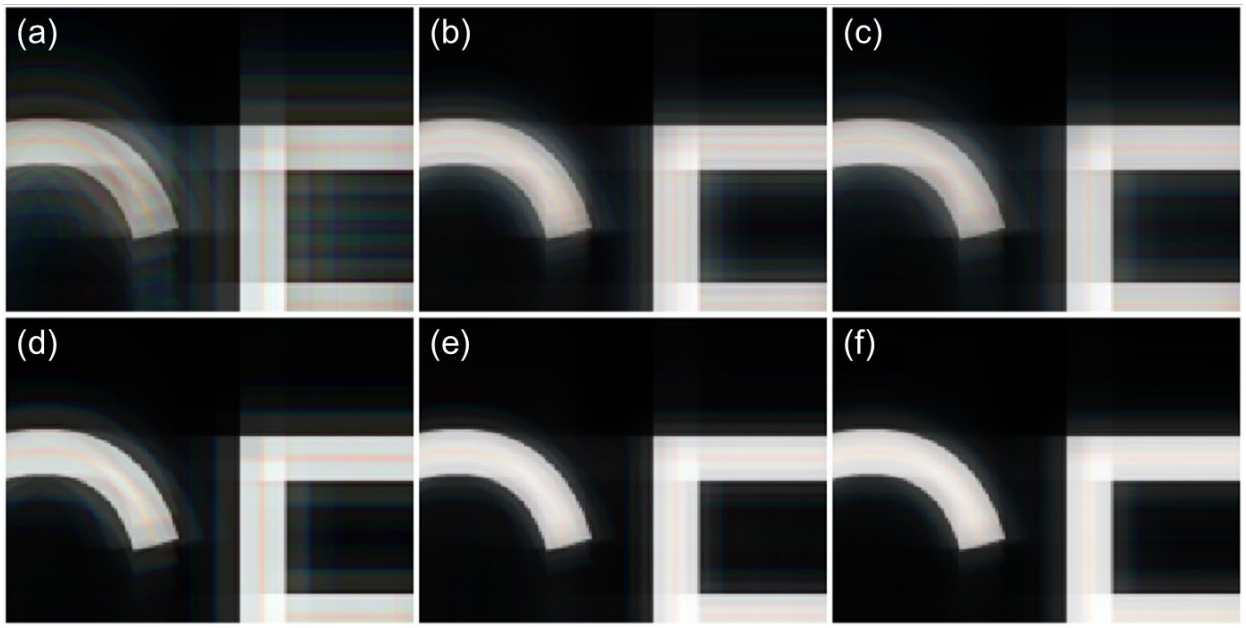

Figure 4 - 9 Diffracted images at aperture ratio 30% (a-c) and 50% (d-f) with unit cell sizes n=1,2,3.

CHAPTER 5 COMPACT FOVEATED AR DISPLAYS WITH POLARIZATION SELECTIVE PLANAR LENSES

The content of this chapter was previously published in [80].

5.1 Background

Thanks to the rapid development of powerful microprocessors, high-pixel density display panels, thin and small formfactor optics, and precise device fabrication capabilities, NEDs have finally come into our lives. Both VR and AR can enhance our perception and interaction with the real world [6,81]. While VR generates a fully immersive, artificial environment for the user to engage with, AR blends digital elements with the user's see-through surroundings. Despite the release of several commercial AR headsets, such as Google Glass, Microsoft HoloLens, and Magic Leap 2, the challenge remains in delivering high-quality images in a compact size that meets consumer’s expectations. The design of such devices should fit the HVS [1] and be compact and lightweight for a comfortable long-term wearing, while minimizing visual fatigue caused by the VAC [19,23,82]. Since the binocular overlapping FoV in HVS is more than 100° and the highest visual acuity is about 30 cycles per degree (cpd, or 60 PPD), the NED should cover a wide FoV while satisfying high angular resolution. However, in a traditional NED, there is often a tradeoff between FoV and angular resolution for a single microdisplay light engine. Commercial products often prioritize wide FoV over high angular resolution, resulting in an annoying screen-door effect. One potential solution is to use a high-resolution panel as the light engine, but to achieve human visual acuity a 6K display panel is required for the 100° FoV. Although it is possible to fabricate such a high pixel-density panel (>3000 pixels per

inch), the production yield, high frame rate (say, 120 Hz), large amount of data transfer, thermal effect, high computational load, and high-power consumption remain technical challenges.

Noticing that the human visual acuity decreases rapidly away from the fovea, the whole FoV can be divided into foveal and peripheral regions, and each part can be rendered in different resolution. The perceived resolution varies across the image, where the foveal region requires a higher pixel density than the peripheral. Foveated displays are conceived based on this characteristic of the HVS. In this way, the huge pixel number requirement and rendering burden is greatly relieved while providing an overall immersive experience to the user. For example, Tan et al. proposed a dual resolution VR system utilizing two display panels with different optical magnification, where the foveated region shifting is achieved by a switchable LC deflector [83]. Kim et al. built an AR system where the foveated region is steered by moving the microdisplay and the eyebox of the Maxwellian peripheral view is expanded by translating the holographic optical element [12]. Lee et al. implemented a two-display-module AR display by combining a holographic foveal display and a peripheral display based on polarization volume lenses and diffusers [84].

Yet, the two employed light engines inevitably take up valuable space in an NED, especially for an eyeglasses-like AR display. Efforts have been made to realize an optically foveated display in a single light engine. Lyu et al. proposed a perceptual-driven approach for designing a statically foveated NED with a wide FoV and minimal image degradation [85]. Yoo et al. designed a VR system including two doublets based on Pancharatnam–Berry phase lenses (PBL), where the light from the same display panel

experiences different optical power according to its polarization state [86]. Similarly, Yin et al. demonstrated a pancake-like foveated VR system with an impressive 4.4x enhancement ratio [87].

In this paper, we propose a Maxwellian-type foveated AR system using a single light engine. The high-resolution foveal image and the low-resolution peripheral image are encoded into the light engine by a temporal polarization-multiplexing method. Two polarization-sensitive off-axis CLC lenses and a PBL are employed to separate the two views. One polarization provides a large FoV while the other realizes a high angular resolution imaging in a small fovea region. Apart from that, the VAC issue does not exist in Maxwellian displays and the aberration can be eliminated for each view by matching the recording and reconstruction signals [40]. The proposed architecture effectively reduces the system volume by employing a single display module and achieves a wide FoV and high perceived angular resolution simultaneously.

5.2 Methods

When a chiral compound is doped into a nematic host, the LC will spontaneously form a helical structure. Within a helical pitch, the CLC directors are reoriented from 0 to 2π. The analysis of LC elastic free energy density reveals that the helical structure with a pitch length P leads to a minimal energy state. Thus, photonic devices based on the helical structure of CLC can be achieved through self-organizing process. According to the helical twist, CLCs can be classified as right-handed CLCs (R-CLC) and left-handed CLCs (L-CLC). If the incident circularly polarized light has the same handedness as the helical twist in the planar CLC, at normal incidence, the light propagating along the helix will experience Bragg reflection, while the opposite handedness component will mostly

pass through the CLC layer. The reflection band spans over a spectral range $n_oP<\lambda<n_eP$, where n_o and n_e are the ordinary and extraordinary refractive indices, respectively. By combining CLCs with a patterned alignment layer, photonic devices with arbitrary phase profiles can be created [88,89]. For examples, an on-axis CLC lens [90,91] is enabled by adopting a parabolic phase profile and a large-angle diffraction grating is realized by a sawtooth phase profile [92–94]. The large scale production of CLC photonic devices can be achieved by the holo-imprinting technique [95,96], empowering cost-effective fabrication. The CLC devices are particularly attractive for AR applications because ~50% of the ambient light with an opposite handedness can pass through [97,98]. More importantly, CLC devices can be stacked together to achieve different functions by the polarization-multiplexing method.

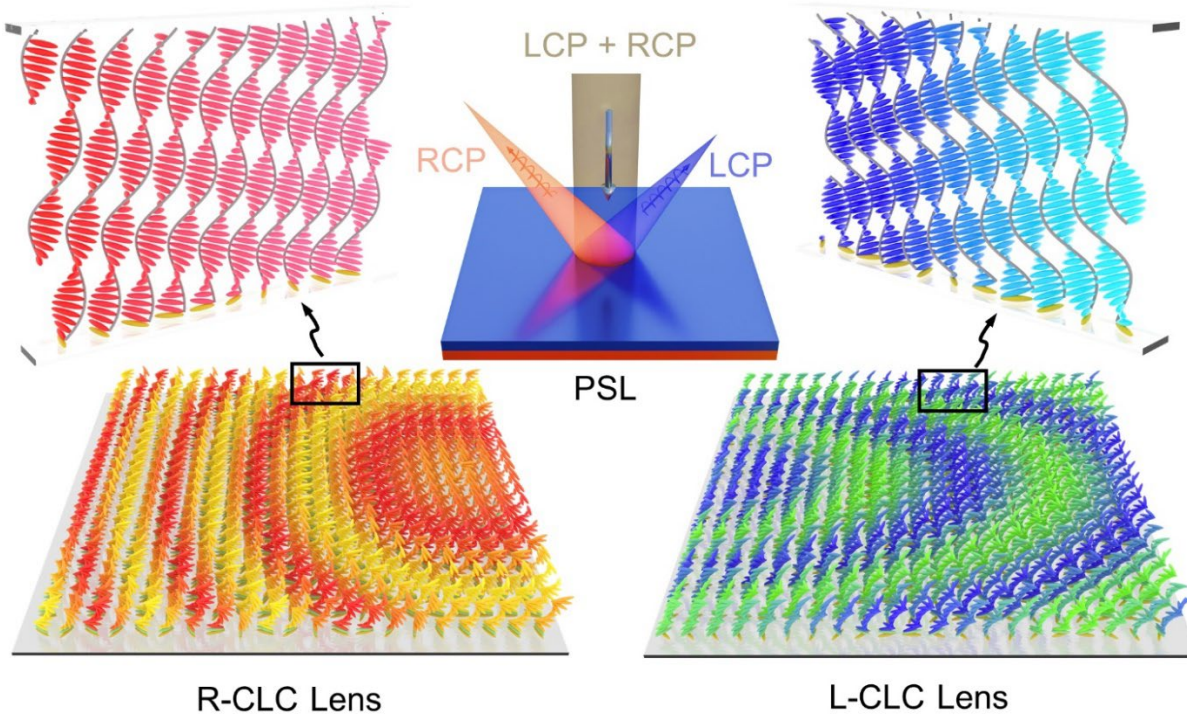

Figure 5 - 1 The functionality of a polarization selective lens (PSL) and its microscopic structure. The PSL consists of two CLC lenses with opposite handedness. When an unpolarized beam hits the PSL, the RCP light converges to a farther spot on the left side while the LCP light converges to a nearer focal point

on the right side. The phase profiles of R-CLC and L-CLC lenses can be observed from the molecular arrangement.

As illustrated in Fig. 5-1, two CLC lenses with orthogonal handedness are stacked into a polarization selective lens (PSL). When an unpolarized beam hits the PSL, the RCP light converges to a farther spot on the left side while the LCP light converges to a nearer focus point on the right side. The phase profiles of R-CLC and L-CLC lenses can be observed from the molecular arrangement. The surface treatment provides CLCs with a spatially varying rotation of the LC optical axis on the substrate. The rotation angle changes continually and form non-centrosymmetric parabolic phase profiles. When zooming into a small portion of the LC director structure, the CLCs are twisted along a slanted axis, and look like a local polarization volume grating [99,100] whose horizontal periods and slanted angles vary spatially. Meanwhile, the CLC twist direction is opposite in the two lenses, which is the origin of the polarization selectivity.

Figure 5-2(a) depicts the system configuration of the proposed Maxwellian-type foveated AR display based on the PSL. The PSL consists of two off-axis CLC lenses, functioning as see-through imaging combiners, which are responsible for the foveal and peripheral views, as shown in Fig. 5-2(b) and Fig. 5-2(c), respectively. By combining the two views, the eye will perceive a complete image like Fig. 5-2(d). The CLC lens for the foveal view is denoted as CLCL-F and the other for the peripheral view is denoted as CLCL-P. The two CLC lenses respond to LCP and RCP lights, respectively. Each lens works in a Maxwellian way and has different effective areas to provide different FoVs, since the FoV is related to the lens area and the distance of eye relief. To ensure all the rays pass through the center of the eye lens, the focal spots of both CLC lenses should be located at the same point. Assuming the light from the LBS is linearly polarized, it is modulated

into a plane-wave-like beam by a collimating lens (CL). The polarization rotator (PR) is composed of a twisted nematic (TN) cell and a QWP film. By controlling the voltage of the TN cell, the PR can select the desired orthogonal circular polarization state in a time sequence. The RCP and LCP lights behave differently when traversing the PBL as they encounter opposite phase profiles. For example, the RCP light experiences a positive power and thus is converged, while the LCP light experiences a negative power and is diverged. After passing through the PBL, the handedness is flipped and the off-axis CLC lenses converge two circularly polarized lights to the center of eye lens, which in turn are projected onto the retina.

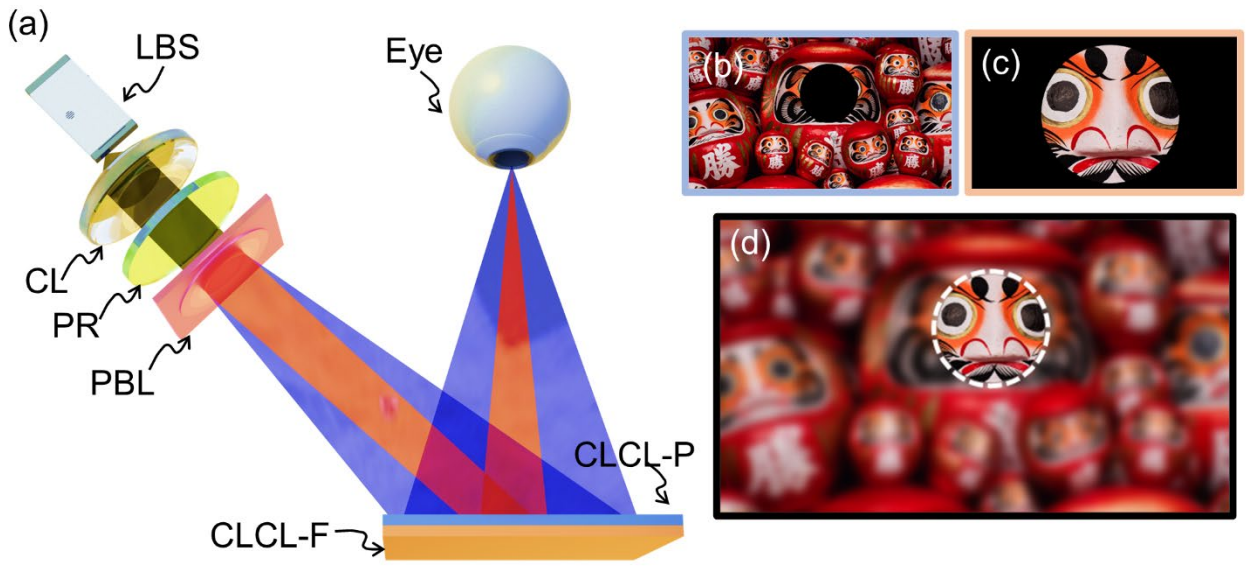

Figure 5 - 2 (a) Sketch of a Maxwellian-type foveated AR display. (b) Input image for peripheral view. (c) Input image for foveated view. (d) Simulated perceived image on the retina. The white dashed lines outline the high-resolution part of an image projected on the foveal region of the retina.

The effective diameter (*D*) of the CLCL-F and the eye relief (ER) jointly determine the foveal FoV (FFoV), as Eq. (5-1) indicates. Similarly, peripheral FoV (PFoV) can be traced back from the effective diameter of the CLCL-P (*D'*) by Eq. (5-2):

$$D = 2 \times ER \times \tan\left(\frac{FFoV}{2}\right), \quad (5-1)$$

$$PFoV = 2 \times \arctan\left(\frac{D'}{2 \times ER}\right), \quad (5-2)$$

5.3 Experiment

In the initial design, the enhancement ratio is set to be about 3. If we choose FFoV=17°, PFoV = 54° and ER=2.0cm, then we can deduce that *D*=0.6cm and *D'*=2cm. An off-the-shelf broadband PBL (Edmund Optics) with a focal length of 12cm at λ=457 nm is selected. In addition, parameters *d*, *θ*, and *h* are set as 6.5cm, 45° and 0.5cm to meet the design requirement.

A common technique for recording such phase patterns is the photo-alignment polarization holography, where the LCP and RCP light beams interfere with each other, projecting a spatially varying linear polarization pattern on the sample. The exposure setup is illustrated in Fig. 5-3(a). The beam from the laser (λ=457 nm, Cobolt Twist) is filtered, expanded, and collimated before sending to the PBS. A half-wave plate is inserted before the PBS to adjust the *s* and *p* component ratio of the beam. Two QWPs are employed to realize the LCP and RCP states. A dielectric mirror directs the beam angle in one of optical paths. A PBL and a template lens (TL) are inserted in each optical path to create the designed phase pattern. The exposure setup is built following reciprocity between the reconstruction and recording processes. Figs. 5-3(b)(c) are the detailed optical path diagrams of CLCL-F and CLCL-P. The TL is a small *f*-number lens (*f*/0.8), and its focal length equals the ER. The separation between the sample and the TL is twice that of ER in Figs. 5-3(b)(c). The acute angle between two optical axes (red dashed lines)

is the complementary angle of θ. The PBL is placed at a distance d from the sample. In Fig. 4-3b, the incident light is RCP. For the exposure setup of CLCL-P, the polarization of incident light is flipped. If the PFoV is set to be symmetric as Fig. 5-3(c) depicts, then the FFoV will be asymmetric. Noticing that both the mirror and PBL will flip the handedness of a circularly polarized light, the polarization of two beams should be orthogonal after QWP_1 and QWP_2.

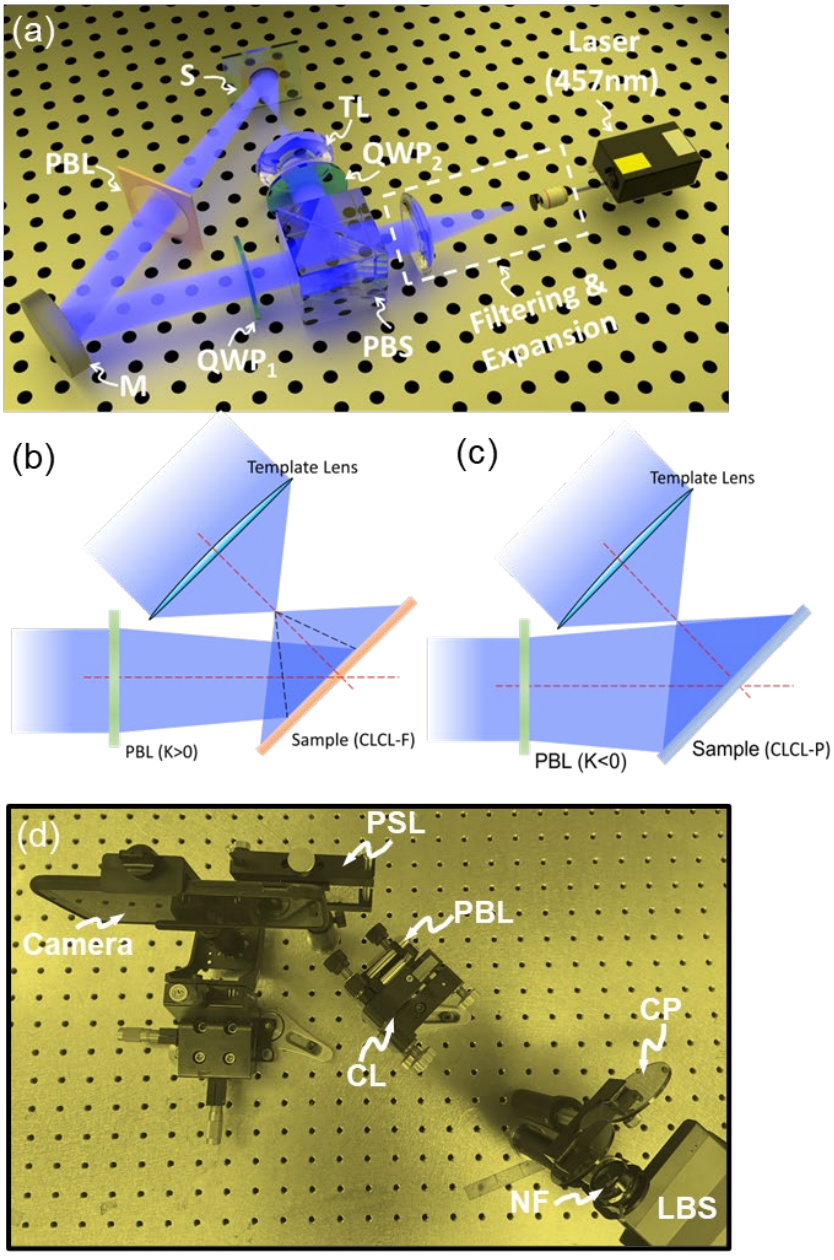

Figure 5 - 3 (a) Exposure setup for generating the phase profile for CLC lenses. Detailed optical path diagram of (b) CLCL-F and (c) CLCL-P. (d)The benchtop demo of the proposed Maxwellian foveated display. M: dielectric mirror. TL: template lens. S: sample. NF: notch filter @ 457nm. CP: circular polarizer.

The interference pattern is then recorded on the sample substrate coated with a photoalignment layer. First, the substrate is cleaned with ethanol, acetone, and isopropyl alcohol. It is then treated with UV-Ozone for 5 minutes. The photoalignment material used is Brilliant Yellow, which is supplied by Tokyo Chemical Industry Co., Ltd. The Brilliant Yellow is dissolved in N,N-dimethyl-formamide at a concentration of 0.2% by weight, and then filtered through a 0.2-μm Teflon syringe filter to remove impurities. After filtration, the Brilliant Yellow solution is spin-coated onto the substrate. The exposure dosage is bout 3J/cm^2 (35mW/cm^2 for 1.5min). Once the exposure is finished, the sample is coated with another layer of CLC mixture. The CLC mixture is made up of 94.28% RM257 (from HCCH), 2.62% chiral dopants R5011 or S5011 (from HCCH), 3% photo-initiator Irgacure 651 (from BASF), and 0.1% surfactant Zonyl 8857A (from Dupont). The composition of R-CLC and L-CLC solvent employed in the lens fabrication is the same except for the handedness of chiral dopants. After that, the CLC mixture is further diluted in toluene at a weight ratio of 1:6, which provides an overall diffraction efficiency of about 60% with the corresponding circularly polarized incident light at λ= 457 nm. The transparency is about 65% with a linearly polarized incident light at 457 nm. The film thickness is about 500 nm measured with a profilometer. The diffraction efficiency is sufficient for an optical combiner in the Maxwellian display. Also, a lower diffraction efficiency is helpful to increase the see-through transmittance after stacking multiple CLC lenses together.

5.4 Results and Discussions

The functionality of the CLCL-F is demonstrated in Fig. 5-4(a). A collimated beam is modulated by a circular polarizer to obtain pure RCP light. The light then passes the PBL employed in the exposure process, transforming into a converging beam, and flipping its handedness. The zeroth order reflection light is focused obeying the law of reflection, and the first-order diffraction beam also focuses to a different spot. When the handedness of incident light is flipped and the off-axis lens is replaced by CLCL-P, as shown Fig. 5-4(b), the beam after the PBL starts to diverge. The diffracted light focuses to the same spot as in Fig. 5-4(a), but with a larger FoV. The light color in Fig. 5-4 is over-saturated and the reflected intensity is about one order of magnitude lower than the diffracted. The zeroth order reflection can be further suppressed by coating an anti-reflection film on the glass substrate.

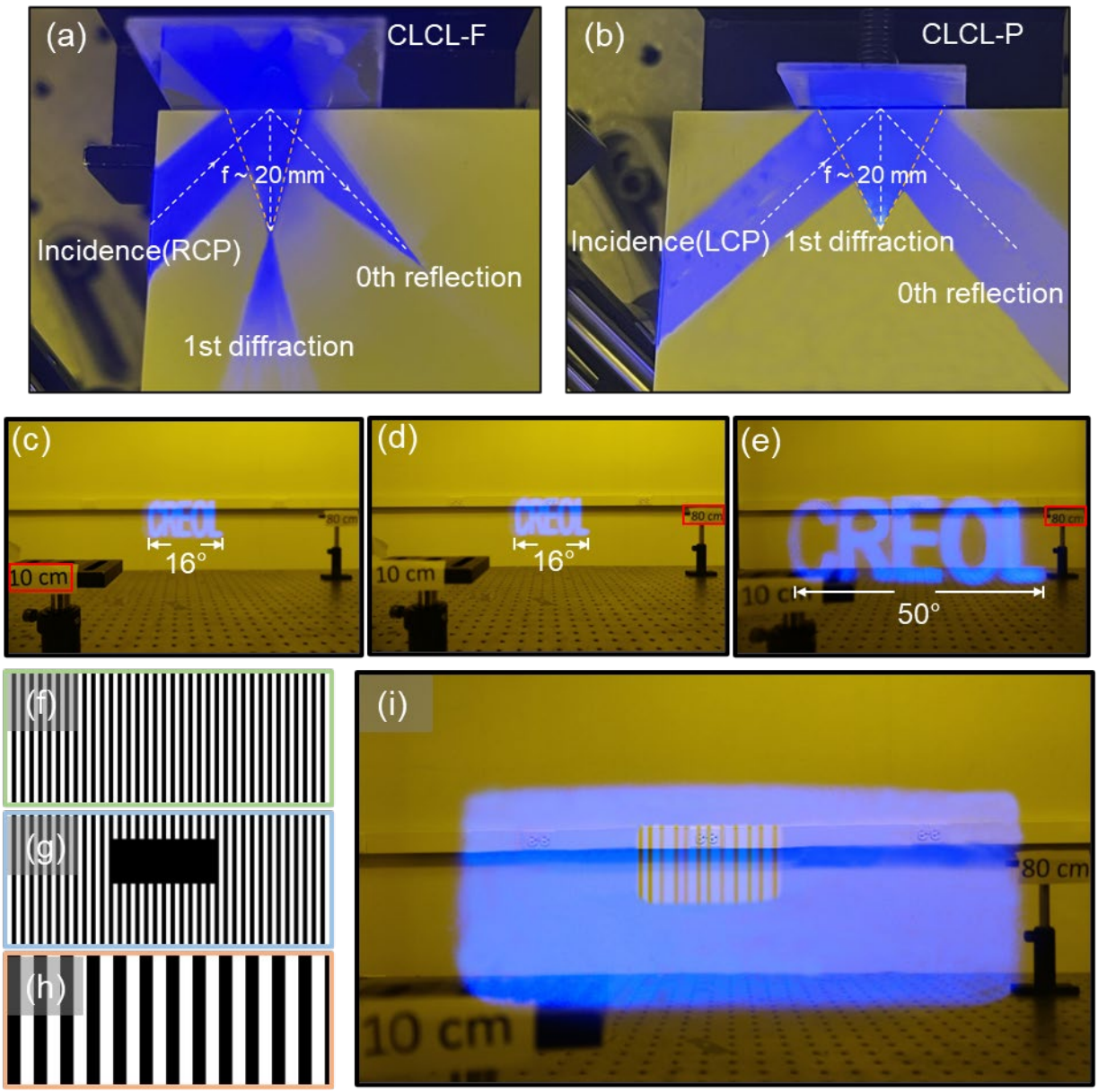

Figure 5 - 4 Photos of (a)CLCL-F and (b)CLCL-P diffracting light. The displayed image is always in focus no matter at (c) near or (d) far depths. The system shows (d) foveal FoV and (e) peripheral FoV for RCP and LCP incident light with same content. The focus depth is indicated by the red box. (f) The test pattern for angular resolution evaluation. (g) Peripheral image. (h) Foveal image. (i) The combined experimental output.

To demonstrate the feasibility of the proposed Maxwellian foveated display, a benchtop demo was built, as illustrated in Fig. 5-3(d). A phone camera (One Plus 5T) was placed at 20 mm in front of the CLC lenses, and its shutter speed was set to 1/15s. Two CLC lenses, responsible for peripheral and foveal FoV respectively, were stacked together.

The polarization of input light from the LBS (SONY, MP-CL1) was manually modulated by two orthogonal circular polarizers. A notch filter (Thorlabs, λ=457nm) was adopted to control the incident light wavelength and reduce its intensity. We chose a telephoto positive lens (*f*=20cm) as the collimation lens. Such a long focal length was adopted to exaggerate the display resolution enhancement effect. In practice, a condenser with an ultrashort focal length could be applied. For the LCP incident light, the collimated light was diverged by the PBL and converted to RCP light. Similarly, the collimated RCP light was converged by the PBL and converted to LCP light. Since the human visual system is very sensitive to the discontinuities in the observed images, blending techniques are required to smoothen the boundary between foveal and peripheral views. As pointed out by Kim et al8, a linear blending algorithm can be applied to both foveal and peripheral images, where a Gaussian blur is applied to match the spatial frequency of two images for achieving a smoother transition.

The displayed image in a Maxwellian display should always stay in focus, regardless of the focal length of the combiner. To examine this characteristic, the incident light is modulated to RCP light. In Figs. 5-4(c)(d), the focal length of the camera is adjusted to near (10cm) and far (80cm) depth, and the displayed images ‘CREOL’ are in focus for both situations. When the incident light is switched to LCP light, a much larger FoV is shown in Fig. 5-4(e). The measured horizontal FoV is 16° for foveal view and 50° for peripheral view. This ratio (≈3.12) agrees well with the 3.18x originally designed enhancement ratio. The image qualities of foveal and peripheral images can be evaluated by the MTF of the imaging system. In the experiment, MTF can be determined by measuring the contrast ratio of bar patterns with different spatial frequencies. A

monochrome 1951 USAF resolution target can be a good display pattern for such measurement.

Although the full horizontal resolution of the LBS used in the experiment is 1920 pixels, the collimation lens with a long focal length allows us to only exploit a small portion of it. With fewer pixels, the image quality between two views can be intuitively evaluated. The actual pixel number implemented is 73(H)×30(V). We designed a test pattern consisting of alternating arranged black and white stripes with equally spaced at one pixel, as shown in Fig. 5-4(f). The corresponding peripheral image and foveal image is demonstrated in Figs. 5-4(g)(h). The position of the foveal view is left empty in Fig. 5-4(g), and this part of image is enlarged ~3x in Fig. 5-4(h) accordingly. Since in the experiment we do not employ a switchable polarization rotator, the polarization state of the incident light is manually modulated by circular polarizers, without synchronization. As a result, the images of peripheral view and foveated view are taken separately by manually changing the displayed contents and incident polarization state, while keeping the camera still. We then crop the foveal region and replace the corresponding pixels in the peripheral image to obtain Fig. 5-4(i). We see that the stripes are fully indistinguishable in the peripheral view. Nevertheless, in foveal view, the stripes can be clearly discerned, despite uneven thickness. The reasons can be fourfold. First, the beam will diverge due to diffraction while propagating. If the beam size gets too large, the display fails to satisfy the resolving power of the human eye. Second, due to the raster scanning mechanism of the LBS, the perceived resolution is lower than the claimed parameters. Third, although the off-axis CLC lenses are fabricated to reconstruct focused beam to the eye pupil without aberration, the employed collimation lens is not ideal. Fourth, there is still some

misalignment in the demo, which cannot reproduce the setup during exposure. To enhance the image quality, an aspherical condenser could give a better plane-wave beam shaping. In addition, there is no need to squeeze out the maximum resolution of the LBS, since the theoretical max foveal angular resolution reaches 60 cpd, which is well beyond the human resolution limit. In addition, although the prototype only demonstrates a single eyebox and monochromatic images, this method is compatible with pupil-steering [40] and full-color AR displays by stacking multiple layers of CLC lenses.

5.5 Conclusion

In this paper, we propose and experimentally demonstrate a Maxwellian foveated AR display based on a single light engine by using a temporal polarization multiplexing method. The optical combiners are two polarization-selective CLC lenses and one PBL for separating the foveal and peripheral views. One CLC lens provides a large FoV while the other realizes a high angular resolution imaging in a small fovea region. The angular resolution of the foveal view is enhanced by 3.12x compared to the peripheral while maintaining a compact form factor. By employing polarization selective planar lenses, the setup of foveated AR displays becomes simpler due to the reduction in the number of panels and optical components, resulting in a more compact, lightweight, aberration-free, and easily integrated system. At the same time, the features of Maxwellian displays are preserved, making the system always-in-focus. This design could find promising applications in various mixed reality display devices.

CHAPTER 6 FULL-COLOR, WIDE FOV SINGLE-LAYER WAVEGUIDE FOR AR DISPLAYS

The content of this chapter was previously published in [101].

6.1 Introduction

Waveguide technologies are becoming increasingly crucial in AR displays, mainly due to their compact form factor and EPE capability. [3,4] Geometric waveguides [102], which employ mirrors and prisms for light coupling, exhibit a minimal wavelength dispersion. This characteristic is particularly advantageous for creating full-color AR displays with a single-layer waveguide. Such a design not only eliminates the misalignment issues [103] but also simplifies the device assembly process. Nevertheless, a significant challenge arises in the complex fabricating process, mainly due to the requirement for cascading these partially reflective mirrors, which complicates the mass production. [104]

In contrast, diffractive waveguides are significantly impacted by the wavelength dispersion. Even though the grating vectors in all couplers are summed to zero, the TIR bandwidth in these waveguides is still dependent on the wavelength. This results in a wavelength-dependent FoV, presenting a limitation in single-layer diffractive waveguides [105]. Therefore, achieving a full-color AR display with a 40°~70° diagonal FoV typically requires two or three waveguides [106]. Common types of diffractive waveguide combiners include Volume Holographic Gratings (VHG) and Surface Relief Gratings (SRG). VHGs operating in the Bragg regime are known for their large diffraction angles and high diffraction efficiency. However, they usually have limited angular and spectral bandwidths, primarily due to their small index modulation contrast [107]. On the other

hand, SRGs offer a greater design flexibility [5]. Yet, fabricating certain surface structures, such as those with a large, slanted angle and high aspect ratio, remains challenging [104].

Recently, PVG has emerged as a new diffractive waveguide combiner [93,108,109]. Operating in the Bragg regime, similar to VHGs, PVGs are distinguished by their LC compositions. Such a material choice allows for a higher index modulation contrast (0.1~0.3), enabling a broader spectral and angular bandwidth. Their unique response to circularly polarized light, a result of the anisotropic nature of liquid crystals and their helix twist direction, introduces a new dimension to waveguide design. Research by Gu et al. has shown that stacking two PVGs, each responding to an orthogonal polarization but with the same horizontal period, can further increase the angular bandwidth [97]. Additionally, the simple fabrication process of PVGs suggests potential for high yield and cost effectiveness. PVGs also provide the advantage of electrically controlled diffraction efficiency with rapid sub-millisecond response time [110]. The possibility of achieving a full-color AR display with a single PVG waveguide has been explored by Ding et al [105]. However, their discussion is primarily focused on the 1D EPE scheme.

Here, we embark on a comprehensive analysis of the FoV limitations in a single-layer waveguide across various EPE schemes. Our discussion delves into the intricate relationship between the FoV limit and the angular response of the waveguide combiner. We then propose a novel approach, utilizing a gradient pitch PVG as an in-coupler in conjunction with a butterfly EPE scheme, aiming to reach the theoretical limit of full-color FoV in a single-layer waveguide. Specifically, we introduce an optimized full-color butterfly EPE scheme, which is designed to achieve a 54.06° diagonal FoV with a 16:10 aspect ratio. To validate our approach, we have designed a PVG that meets the requirements of

this in-coupler and have thoroughly analyzed the potential FoV crosstalk issues. This analysis is supported by ray tracing simulations, demonstrating the feasibility and effectiveness of our proposed design.

6.2 EPE schemes

Waveguide-based AR displays, while highly valued for their compact formfactor and EPE capabilities, confront several challenges, including reduced light efficiency, inadequate color uniformity, and compromised FoV. Besides refractive index, several factors also significantly influence the FoV. In this section, we investigate the factors affecting the FoV of a single-layer waveguide, particularly focusing on how different EPE schemes impact these constraints.

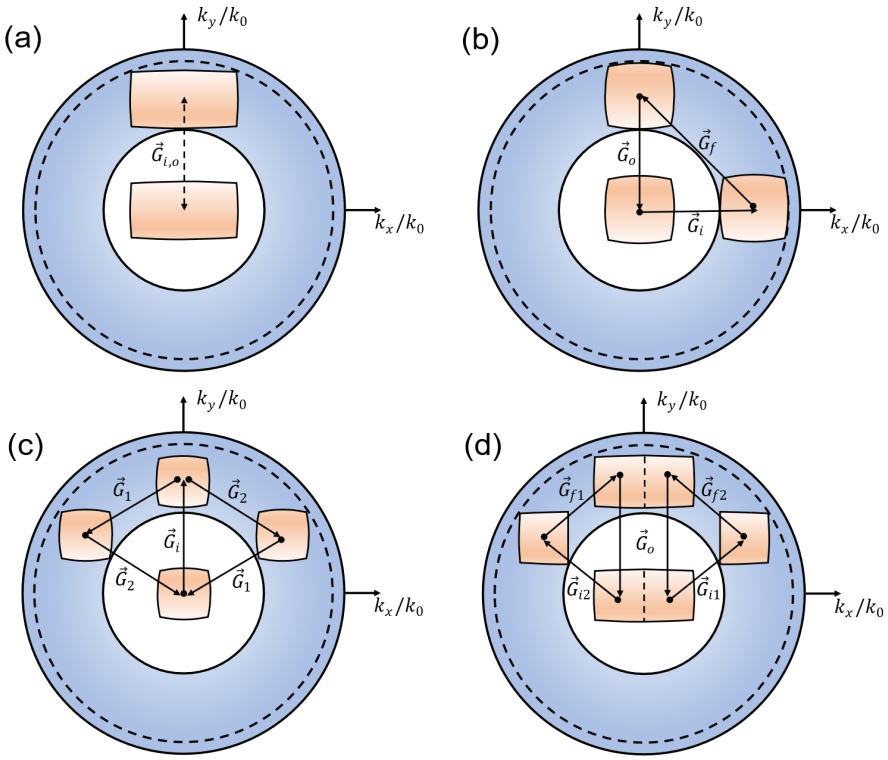

Figure 6 - 1 Sketch of EPE schemes in k-vector diagrams. (a) 1D. (b) 1D+1D. (c) 2D. (d) Butterfly.

Fig. 6-1(a-d) illustrates four k-vector diagrams for various EPE schemes [4]. In these diagrams, the inner circle represents the critical angle of TIR, and the dashed-line circle marks the maximum allowable propagation angle. During TIR propagation, the FoV, depicted as an enclosed box, must remain within the annular region between these two circles.

In the 1D EPE scheme, there are only two grating vectors: one for the in-coupler $\vec{G}_i$ and another for the out-coupler $\vec{G}_o$. Although these vectors have the same magnitude, they are opposite in direction, as shown in Fig. 6-1(a). This arrangement allows for the largest possible FoV, but the tradeoff is the increased form factor. In the 1D EPE scheme, since EPE occurs only in one direction, the input coupler for the other direction must be significantly larger to meet the eyebox requirements [106]. This substantial increase in size is a key reason why the 1D EPE scheme is not commonly adopted in practical applications.

The 1D+1D EPE scheme offers a proper compromise between FoV and form factor. Illustrated in Fig. 6-1(b), this scheme employs three grating vectors: $\vec{G}_i$ for the in-coupler, $\vec{G}_f$ for a secondary grating, and $\vec{G}_o$ for the out-coupler, together forming an enclosed triangle. In this configuration, the FoV is constrained because it has to fit within two distinct positions in the annular region, resulting in a smaller FoV compared to that of the 1D EPE scheme. However, the advantage of this scheme lies in its two-directional exit pupil expansion, allowing for a smaller in-coupler than what is required in the 1D EPE scheme. This efficient utilization of space, balancing FoV with a more compact form factor,

contributes to the widespread adoption of the 1D+1D EPE scheme in practical applications.

To further reduce the waveguide's form factor, the 2D EPE scheme has been proposed. This scheme, while similar to the 1D EPE approach in having one in-coupler and one out-coupler, distinguishes itself by utilizing a 2D grating for the out-coupler. The grating vectors, $\vec{G}_1$ and $\vec{G}_2$, enable the 2D grating to simultaneously expand the exit pupil in two directions and out-couple the light. However, despite this advancement, the FoV in the 2D EPE scheme is still subjected to similar limitations as observed in the 1D+1D EPE scheme. This constraint is illustrated in Fig. 6-1(c).

To extend the maximum achievable FoV, the butterfly EPE scheme has been introduced and implemented in Microsoft's HoloLens 2. This innovative approach is depicted in Fig. 6-1(d), where the FoV is divided into two separate portions, each managed by its own in-coupler. This design allows each in-coupler to handle a distinct half of the FoV. The scheme then utilizes two folded gratings, each responsible for either the positive or negative part of the FoV. Working in concert, these gratings expand the overall FoV substantially. The two separate FoV segments are then seamlessly integrated, allowing the butterfly EPE scheme to ingeniously bypass FoV limitations while preserving the advantages of 2D EPE.

6.3 Asymmetric angular response of PVG

In AR displays, the FoV is generally expected to be symmetric around 0°. However, Bragg gratings, which are characterized by their high efficiency at a particular diffraction order,

exhibit an asymmetric angular response. This asymmetry is also a trait of PVG, which is a specific type of Bragg grating.

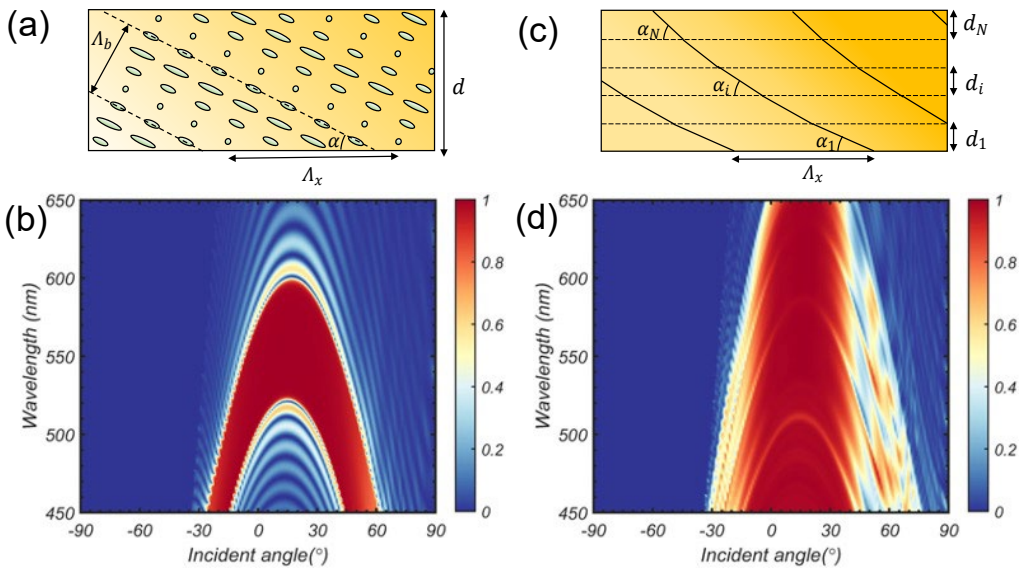

Figure 6-2 (a) The LC orientation of a uniform-pitch PVG. (b) Plot of relation between wavelength-incident angle and diffraction efficiency of a uniform-pitch PVG. (c) The structure of a gradient-pitch PVG. Bragg surfaces in each sublayer are labeled. (d) Plot of relation between wavelength-incident angle and diffraction efficiency of a gradient-pitch PVG.

The molecular structure of PVG, as shown in Fig. 6-2(a), is determined by its horizontal period Λ_x and the slanted angle α, where α represents the tilt of the Bragg plane relative to the horizontal direction. In the spectral and angular space, the high diffraction efficiency band follows a parabola-like trajectory. This is depicted in Fig. 6-2(b), which shows the diffraction efficiency for a PVG with Λ_x = 650 nm and α= 15.62°. Here, n_o and n_e are set to be 1.5 and 1.7, respectively, with a PVG thickness of 2 μm. Both the incident and output media have refractive indices of n_{eff}. Notably, while the angular response of the PVG is asymmetric with respect to 0°, it is symmetric around 15°. Generally, its axis of symmetry is given by $\theta = \arcsin(n_{\text{eff}} \sin \alpha)$, which is usually not aligned at 0°. This characteristic

presents a limitation in achieving the maximum FoV in waveguide-based AR displays, explaining why PVG does not reach its theoretical limit in the 1D EPE scheme.

Like CLC, the spectral response of PVGs can be enhanced by introducing gradient pitches. In this approach, a gradient-pitch PVG can be divided into N sublayers, as Fig. 6-2(c) depicts. While each sublayer maintains the same Λ_x, α varies from α_1 to α_N, with each sublayer having a thickness of d_i. One method to achieve this gradient pitch involves doping the CLC mixture with UV dye [111], followed by exposure to UV light. This process induces a gradient in the chiral dopant concentration. Alternatively, a multiple spin-coating technique [112] can be employed to create gradient pitch CLC, where each sublayer is given a different chiral dopant concentration. The effectiveness of this method is demonstrated in Fig. 6-2(d), which displays the diffraction efficiency of a 5-sublayer PVG. This configuration shows a high diffraction efficiency across the entire visible spectrum, from 0° to 30°. In comparison with the PVG presented in Fig. 6-2(b), the slanted angles for the five sublayers are set at 13°, 14.9°, 16.1°, 17.1°, and 18°, respectively, with each sublayer being 2μm thick. Although this method effectively broadens the angular response of the PVG [113,114], it is important to note that the response remains asymmetric due to the inherent nature of PVG. Consequently, despite the broadening, the effective angular bandwidth that can be utilized in AR waveguides is still limited.

6.4 Optimization of butterfly EPE scheme

In the butterfly EPE scheme, as previously described, the in-coupler is divided into two segments, each responsible for one half of the FoV. This division effectively relaxes the stringent requirements on the angular response of the in-coupler. As a result, a gradient-pitch PVG, despite exhibiting a single-sided angular response across the visible

spectrum, can reach its theoretical full color FoV limit in this configuration. To achieve this, two gradient-pitch PVGs with opposite polarization response are utilized as in-couplers, with each one addressing a specific segment of the FoV. An important aspect of this setup involves a carefully designed optimization process to determine the appropriate grating vectors. If the grating vector of the in-coupler is chosen to be along the x direction, and the grating vector of the out-coupler to be along the y direction, then the following constraints (Eq. (6-1)) should be satisfied on all the available k vectors:

$$1 \le (k_x/k_0)^2 + \left(k_y/k_0 + K_y/k_0\right)^2 \le n_g^2 \sin\theta_{max}^2 , \qquad (6-1)$$

$$1 \le (k_x/k_0 + K_x/k_0)^2 + \left(k_y/k_0\right)^2 \le n_g^2 \sin\theta_{max}^2,$$

where K_x and K_y are the grating vectors of the in-coupler and out-coupler, respectively. These constraints should be satisfied by the minimum and maximum wavelengths of the full color spectrum. The objective function is set to maximize the diagonal FoV (DFoV). To determine the maximum DFoV for each aspect ratio, a nonlinear optimization process is employed. The aspect ratio *m* is defined as $\tan(\mathrm{HFoV}/2) / \tan(\mathrm{VFoV}/2)$. In this study, we utilize MATLAB's fmincon function, a tool for solving constrained nonlinear optimization problems, to find the optimal values. For example, setting n_g = 2.0, θ_{max} = 75° and *m* =16:10, we arrive at the results shown in Fig. 6-3(a). The maximum FoV is 46.79°(H) × 30.26°(V) × 54.06°(D) with λ_{min} = 467.5nm and λ_{max} = 612.5nm. As for the grating periods, the required in-coupler has a Λ_x of 334.5 nm, while the out-coupler's Λ_x is 370.7 nm. For the folded grating, Λ_x is 248.3 nm.

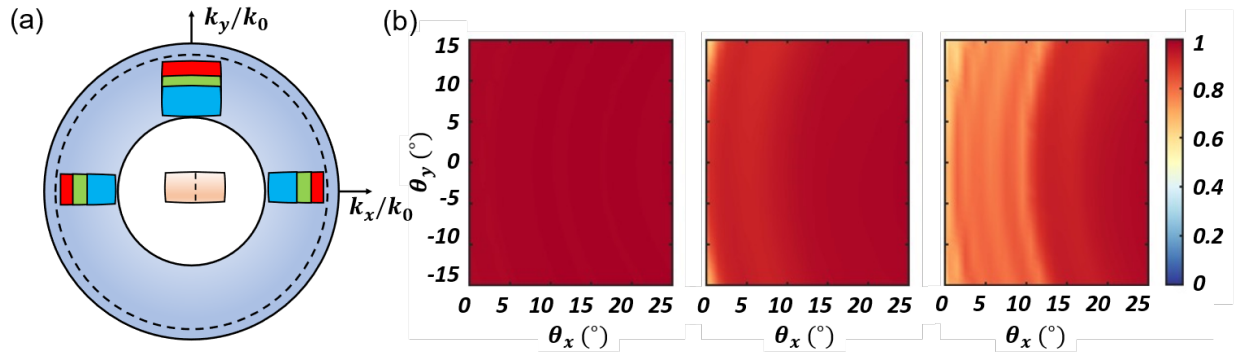

Figure 6 - 3 (a) The optimized butterfly EPE scheme in a k-vector diagram. (b) Plot of diffraction efficiency vs. FoV in air at RGB wavelengths (From left to right: 470 nm, 550 nm, and 610 nm).

The optimization of the gradient-pitch PVG involves adjusting the slanted angle of each sublayer while keeping their thickness uniform. Through this optimization process, it has been determined that a configuration of six sublayers can meet the in-coupler requirements for the butterfly EPE scheme. The slanted angles for these six sublayers are set at 21.0°, 24.2°, 26.3°, 28.0°, 29.6°, and 31.0°, respectively, with each sublayer having a thickness of 1.67μm. Fig. 6-3(b) illustrates the diffraction efficiency of this optimized PVG at three primary wavelengths: 470 nm, 550 nm, and 610 nm. Notably, the diffraction efficiency spans a range of 0° to 25° horizontally and −15° to 15° vertically across these wavelengths. This comprehensive coverage makes the device suitable for use in the butterfly EPE scheme, realizing the theoretical FoV limit in a single-layer waveguide. Such optimization underscores the potential of gradient-pitch PVG in enhancing the performance of AR displays.

6.5 FoV crosstalk analysis

In the optimized butterfly EPE scheme, a potential issue is FoV crosstalk, where the in-coupler designed for one half of the FoV might inadvertently couple light from the other

half, leading to a degradation in image quality. To assess and mitigate this issue, we developed a ray tracing model using LightTools, as depicted in Fig. 6-4(a). In this model, the waveguide thickness is set at 0.7mm. The in-couplers, denoted as I_+ and I_-, are centrally placed in the waveguide, each measuring 1 mm × 1 mm. I_+ handles the left half of the FoV, while I_- manages the right half. Correspondingly, two out-couplers O_+ and O_-, are positioned on the left and right sides of the waveguide to couple out their respective halves of the FoV. The out-coupled light is then focused by two ideal lenses with an 18-mm focal length and captured by plane receivers measuring 7.79mm × 4.87mm. Additionally, an unpolarized light source (S), sized 4.33mm × 2.70mm, is positioned at 5-mm away from the waveguide. An ideal in-coupling lens is laminated to the waveguide. To reduce crosstalk between the left and right halves of the FoV, a left-handed circular polarizer is attached to the left half of the display panel, and a right-handed circular polarizer is affixed to the right half. This setup effectively creates two parallel 1D EPE waveguides. By analyzing the light collected from the two out-couplers, we can evaluate both the in-coupling capability and the extent of FoV crosstalk.

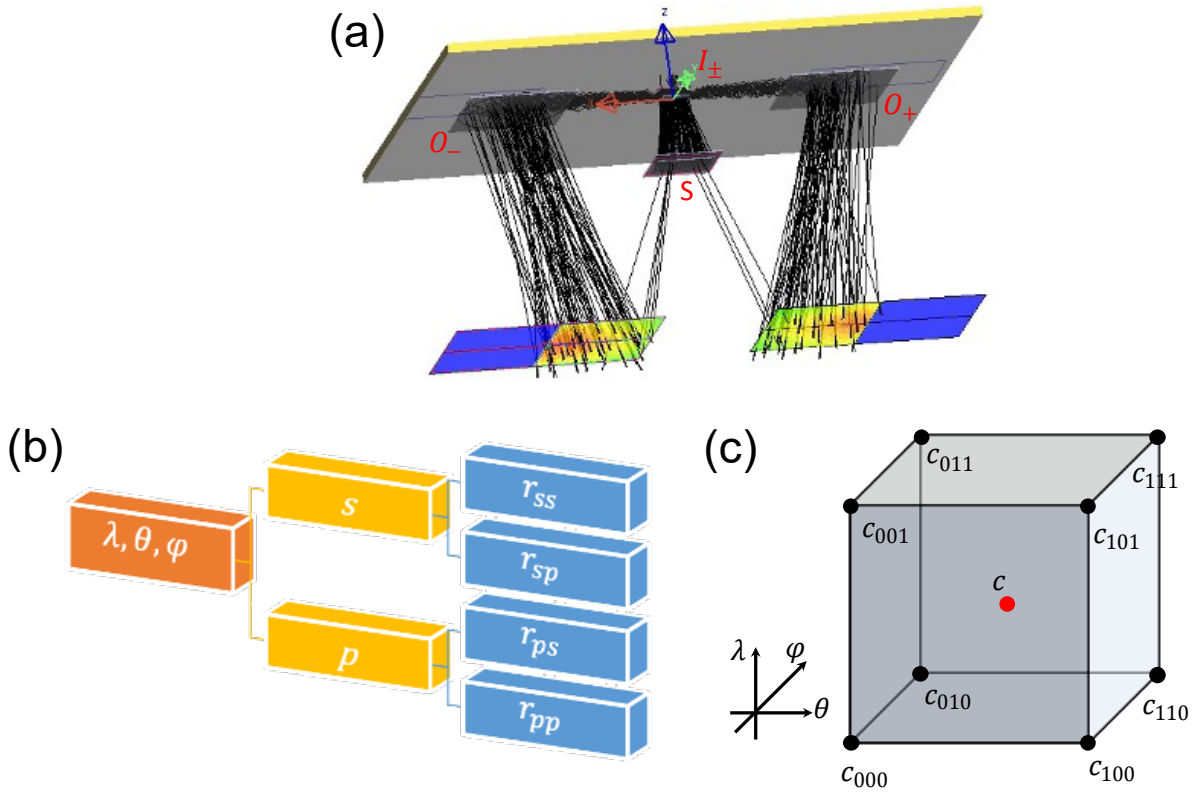

Figure 6 - 4 (a) Sketch of the ray tracing model for analyzing FoV crosstalk issue. (b) Flowchart of generating BSDF data for one reflected diffraction order. (c) Structure of the lookup table and trilinear interpolation method.

In the ray-tracing model, the optical properties of the two out-couplers are ideally set to achieve 100% diffraction efficiency. For the in-couplers, we use the specifically designed PVG, where I_+ responds to LCP light and I_- to RCP light. To accurately model the PVG's behavior, we pre-calculate its bi-directional scattering distribution function (BSDF) using a custom RCWA code. As illustrated in Fig. 6-4(b), the BSDF data generation involves illuminating the PVG with *s* and *p* polarization plane waves at each wavelength λ and incident angle (θ, φ), and then recording the reflected and transmitted electric fields across various diffraction orders. The output electric field is also recorded as *s* and *p* components, defined in their local coordinate system. Due to the anisotropy of the PVG, the *s*-polarized incident light can generate diffracted light with both *s* and *p* polarizations.

For instance, in the BSDF data, a term like r_{sp} represents the *p*-polarized component of the reflected electric field for the *s*-polarized incident light.

To streamline the ray-tracing simulation in LightTools, we employ a lookup table method for interpolating the BSDF data. This approach, depicted in Fig. 6-4(c), involves storing the BSDF data in a 3D lookup table, with dimensions corresponding to $\lambda, \theta, and\ \varphi$. During the simulation, trilinear interpolation is applied in real-time based on the given wavelength and incident angle. Energy conservation is ensured by adjusting the ray's energy according to the diffraction efficiency. Compared to running RCWA simulations in real-time, this method significantly speeds up the process. We have implemented the lookup table approach in LightTools as a dynamic linked library (DLL), enhancing the efficiency of our ray tracing simulations.

In our study, we explored two different configurations for arranging the in-couplers in the butterfly EPE scheme, shown in Fig. 6-5(a-b). The first option involves stacking the two in-couplers together, as depicted in Fig. 6-5(a). Fig. 6-5(c) shows the spatial luminance collected from the out-coupler O_+, which corresponds to the left half of the FoV, at wavelengths of 470nm, 550nm, and 610nm, respectively. While this design effectively covers the left half of the FoV, there is noticeable light leakage into the right half. We define the 'leakage ratio' as the ratio of total luminance in the right half of the FoV to that in the left half. At 470 nm, 550 nm, and 610 nm, the leakage ratios are 8%, 4%, and 1%, respectively. The reason is that although the polarization state of the light from the right half FoV is RCP, the light is still partially diffracted by the LCP PVG and coupled out by the out-coupler O_+. The crosstalk is particularly severe at 470 nm, because the TIR condition is easier to satisfy at a shorter wavelength.

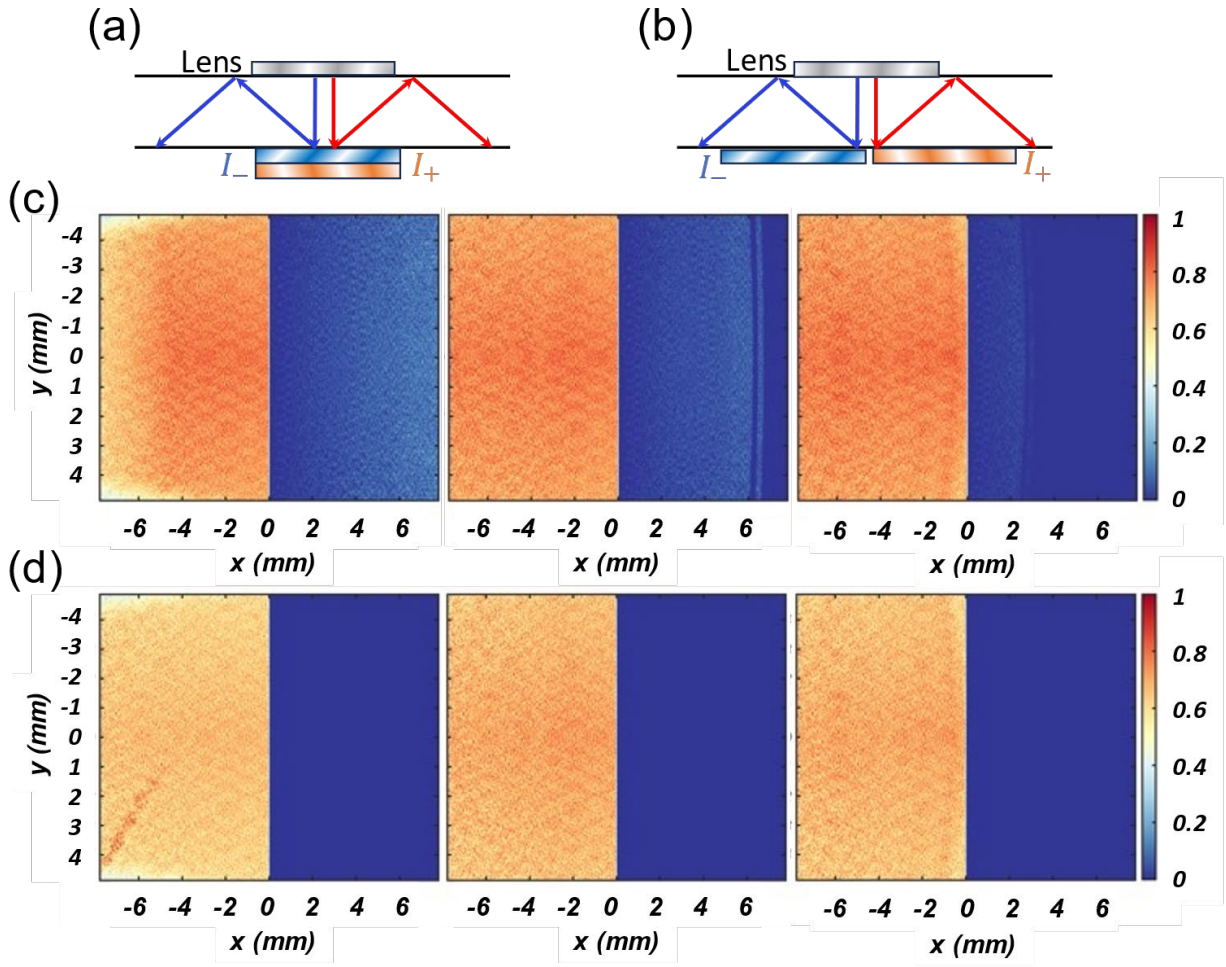

Figure 6 - 5 Configurations of in-couplers in the butterfly EPE scheme and their associated spatial luminance profiles at RGB wavelengths. (a) In-couplers in a stacked configuration. (b) In-couplers separated by 0.5 mm. The corresponding spatial luminance profiles are shown for (c) the stacked configuration and (d) the 0.5 mm separated configuration, at wavelengths from left to right: blue (470 nm), green (550 nm), and red (610 nm).

The second configuration, shown in Fig. 6-5(b), separates the two in-couplers by a 0.5-mm gap. The spatial luminance from O_+ under this arrangement, indicates a significant reduction in crosstalk, with leakage ratios at all three wavelengths falling below 0.1%, as illustrated by Fig. 6-5(d). In this design, it is crucial to align the emission cone of the display panel precisely with the in-coupler positions. For the simulation, we adjusted the aim region of the left and right parts of the light source by 0.75 mm to the left and right,

respectively. This adjustment effectively aligns the display panel's emission with the separated in-couplers, resulting in greatly reduced crosstalk.

6.6 Conclusion

We have conducted a thorough analysis of the FoV limitations in a single-layer, full-color waveguide-based AR display. We discovered that the FoV limit is influenced not only by the refractive index of the waveguide but also significantly by the EPE scheme and the angular response of the waveguide combiner. To mitigate these factors, we proposed to use gradient-pitch PVGs in conjunction with a butterfly EPE scheme. This innovative approach enables the achievement of the theoretical FoV limit. Specifically, we developed an optimized butterfly EPE scheme capable of providing a DFoV of 54.06° with a 16:10 aspect ratio. Additionally, we optimized the in-coupler PVGs for this scheme and constructed a ray tracing model to assess the system's performance, particularly focusing on mitigating the FoV crosstalk issue.

CHAPTER 7 SUMMARY

In the fast-evolving field of display technology, augmented reality stands at the forefront, merging the virtual with the real world in unprecedented ways. This dissertation ventures into the cutting-edge territory of AR display technology, highlighting the obstacles faced by existing systems, including issues with transparent and near-eye displays, and proposes novel solutions aimed at enhancing both the user experience and display efficacy. Centering on pivotal challenges such as minimizing diffraction-induced image blur, resolving the resolution-FoV tradeoff in near-eye displays, and expanding the FoV in waveguide-based displays, this body of work introduces innovative evaluation methodologies, optimization strategies, and design paradigms.

Initially, the research offers a detailed quantitative analysis of the impact of diffraction on background clarity, leading to the formulation of an optimization technique for pixel structures. This technique is specifically designed to reduce diffraction in transparent displays characterized by small aperture ratios, thereby significantly improving image sharpness and visibility. Such advancements are crucial for the practical application of AR in transparent displays.

Subsequently, the dissertation unveils a groundbreaking Maxwellian-type foveated AR system, powered by a singular light engine. This inventive system utilizes a temporal polarization-multiplexing technique to concurrently encode high-resolution images for the foveal area and low-resolution imagery for the peripheral vision, all through one light engine. By integrating polarization-selective lenses, the system adeptly segregates these dual views, offering an extensive FoV and heightened angular resolution for the foveal

region. This effectively diminishes the compromise between resolution and FoV commonly encountered in near-eye displays.

Moreover, the study conducts an in-depth examination of FoV constraints within single-layer waveguides and introduces a novel approach by merging a gradient-pitch polarization volume grating with a butterfly exit-pupil expansion mechanism. This innovative strategy seeks to broaden the FoV in single-layer waveguides up to the theoretical full-color limit, addressing key limitations in waveguide-based AR displays.

Through this comprehensive research, the dissertation aims to tackle fundamental issues in AR display technology, marking a significant advancement towards the development of more immersive and user-friendly AR systems. The proposed methods and designs have the potential to revolutionize AR displays, paving the way for their broader adoption and application in merging digital information with the physical world.

APPENDIX: STUDENT PUBLICATIONS

Journal Publications

[1] Q. Yang, Y. Ding, and S. T. Wu, "Full-color, wide FoV single-layer waveguide for AR displays," J. Soc. Inf. Disp. (2024). (Under review)

[2] Y. Ding, Q. Yang, Y. Li, Z. Yang, Z. Wang, H. Liang, and S. T. Wu, "Waveguide-based augmented reality displays: perspectives and challenges," eLight 3, 24 (2023).

[3] Y. Qian, Z. Yang, E. L. Hsiang, Q. Yang, K. Nilsen, Y. H. Huang, K. H. Lin, and S. T. Wu, "Human Eye Contrast Sensitivity to Vehicle Displays under Strong Ambient Light," Crystals 13, 1384 (2023).

[4] Q. Yang, Y. Li, Y. Ding, and S. T. Wu, "Compact Foveated AR Displays with Polarization Selective Planar Lenses," ACS Appl. Opt. Mater. (2023). https://doi.org/10.1021/acsaom.2c00203

[5] Y. Li, J. Semmen, Q. Yang, and S. T. Wu, "Switchable polarization volume gratings for augmented reality waveguide displays," J. Soc. Inf. Disp. 31, 328–335 (2023).

[6] Y. Ding, Y. Li, Q. Yang, and S. T. Wu, "Design optimization of polarization volume gratings for full-color waveguide-based augmented reality displays," J. Soc. Inf. Disp. 31, 380–386 (2023).

[7] E. L. Hsiang, Z. Yang, Q. Yang, P. C. Lai, C. L. Lin, and S. T. Wu, "AR/VR light engines: perspectives and challenges," Adv. Opt. Photon. 14, 783–861 (2022).

[8] K. Yin, E. L. Hsiang, J. Zou, Y. Li, Z. Yang, Q. Yang, P. C. Lai, C. L. Lin, and S. T. Wu, "Advanced liquid crystal devices for augmented reality and virtual reality displays: principles and applications," Light Sci. Appl. 11, 161 (2022).

[9] J. Xiong, Q. Yang, Y. Li, and S. T. Wu, "Holo-imprinting polarization optics with a reflective liquid crystal hologram template," Light Sci. Appl. 11, 54 (2022).

[10] Q. Yang, Z. Yang, Y. F. Lan, and S. T. Wu, "Low-diffraction transparent micro light-emitting diode displays with optimized pixel structure," J. Soc. Inf. Disp. 30, 395–403 (2022).

[11] Y. Li, Q. Yang, J. Xiong, K. Yin, and S. T. Wu, "3D displays in augmented and virtual realities with holographic optical elements [Invited]," Opt. Express 29, 42696–42712 (2021).

[12] Y. Li, Q. Yang, J. Xiong, K. Li, and S. T. Wu, "Dual-depth augmented reality display with reflective polarization-dependent lenses," Opt. Express 29, 31478–31487 (2021).

[13] C. Spiess, Q. Yang, X. Dong, V. G. Bucklew, and W. H. Renninger, "Chirped dissipative solitons in driven optical resonators," Optica 8, 861–869 (2021).

[14] M. Y. Deng, E. L. Hsiang, Q. Yang, C. L. Tsai, B. S. Chen, C. E. Wu, M. H. Lee, S. T. Wu, and C. L. Lin, "Reducing Power Consumption of Active-Matrix Mini-LED Backlit LCDs by Driving Circuit," IEEE Transactions on Electron Devices 68, 2347–2354 (2021).

[15] J. Zou, Z. He, Q. Yang, K. Yin, K. Li, and S. T. Wu, "Large-angle two-dimensional grating with hybrid mechanisms," Opt. Lett. 46, 920–923 (2021).

[16] J. Zou, Q. Yang, E. L. Hsiang, H. Ooishi, Z. Yang, K. Yoshidaya, and S. T. Wu, "Fast-Response Liquid Crystal for Spatial Light Modulator and LiDAR Applications," Crystals 11, 93 (2021).

[17] E. L. Hsiang, Z. Yang, Q. Yang, Y. F. Lan, and S. T. Wu, "Prospects and challenges of mini-LED, OLED, and micro-LED displays," J. Soc. Inf. Disp. 29, 446–465 (2021).

[18] E. L. Hsiang, Q. Yang, Z. He, J. Zou, and S. T. Wu, "Halo effect in high-dynamic-range mini-LED backlit LCDs," Opt. Express 28, 36822–36837 (2020).

[19] Q. Yang, J. Zou, Y. Li, and S. T. Wu, "Fast-Response Liquid Crystal Phase Modulators with an Excellent Photostability," Crystals 10, 765 (2020).

[20] X. Dong, Q. Yang, C. Spiess, V. G. Bucklew, and W. H. Renninger, "Stretched-Pulse Soliton Kerr Resonators," Phys. Rev. Lett. 125, 033902 (2020).

Conference Publications

[1] Q. Yang, Y. Ding, and S. T. Wu, "Full-color, wide FoV single waveguide AR displays leveraging polarization multiplexing reflective polarization holograms," Proc. SPIE. (2024).

[2] Y. Li, J. Semmen, Q. Yang, and S. T. Wu, "Switchable polarization volume gratings for augmented reality waveguide displays," J. Soc. Inf. Disp. **31**, 328–335 (2023).

[3] Y. Ding, Y. Li, Q. Yang, and S. T. Wu, "68-2: Distinguished Student Paper: Design optimization of polarization volume gratings for full-color waveguide-based AR displays," SID Symp. Dig. Tech. Pap. **54**, 966–969 (2023).

[4] Q. Yang, J. Zou, H. Ooishi, Z. Yang, K. Yoshidaya, and S. T. Wu, "P-90: Student Poster: High Birefringence Liquid Crystal for Fast-Response Phase Modulators," SID Symp. Dig. Tech. Pap. **52**, 1416–1419 (2021).

[5] E. L. Hsiang, Q. Yang, Z. He, J. Zou, and S. T. Wu, "47-4: Student Paper: Ambient Light and Human Vision Effects on High-Dynamic-Range Displays," SID Symp. Dig. Tech. Pap. **52**, 646–649 (2021).

[6] E. L. Hsiang, Y. Huang, Q. Yang, and S. T. Wu, "10-1: Invited Paper: High Dynamic Range Mini-LED and Dual-Cell LCDs," SID Symp. Dig. Tech. Pap. **51**, 115–118 (2020).

[7] Q. Yang, C. Spiess, V. G. Bucklew, and W. H. Renninger, "Stretched-Pulse Solitons in Driven Fiber Resonators," in Conference on Lasers and Electro-Optics (2019), Paper SF1L.3 (Optica Publishing Group, 2019), p. SF1L.3.

[8] C. Spiess, Q. Yang, V. G. Bucklew, and W. H. Renninger, "Highly-Chirped Solitons in Driven Resonators," in Conference on Lasers and Electro-Optics (2019), Paper SF1L.4 (Optica Publishing Group, 2019), p. SF1L.4.

REFERENCES

[1] E. L. Hsiang, Z. Yang, Q. Yang, P. C. Lai, C. L. Lin, and S. T. Wu, "AR/VR light engines: perspectives and challenges," Adv. Opt. Photon. **14**, 783–861 (2022).

[2] J. F. Wager, "Transparent Electronics," Science **300**, 1245–1246 (2003).

[3] J. Xiong, E. L. Hsiang, Z. He, T. Zhan, and S. T. Wu, "Augmented reality and virtual reality displays: emerging technologies and future perspectives," Light Sci. Appl. **10**, 216 (2021).

[4] Y. Ding, Q. Yang, Y. Li, Z. Yang, Z. Wang, H. Liang, and S. T. Wu, "Waveguide-based augmented reality displays: perspectives and challenges," eLight **3**, 24 (2023).

[5] B. C. Kress, *Optical Architectures for Augmented-, Virtual-, and Mixed-Reality Headsets* (SPIE, 2020).

[6] C. Chang, K. Bang, G. Wetzstein, B. Lee, and L. Gao, "Toward the next-generation VR/AR optics: a review of holographic near-eye displays from a human-centric perspective," Optica **7**, 1563–1578 (2020).

[7] H. Kim, Y. T. Kwon, H. R. Lim, J. H. Kim, Y. S. Kim, and W. H. Yeo, "Recent Advances in Wearable Sensors and Integrated Functional Devices for Virtual and Augmented Reality Applications," Adv. Funct. Mater **31**, 2005692 (2021).

[8] H. G. Kim, H. T. Lim, and Y. M. Ro, "Deep Virtual Reality Image Quality Assessment With Human Perception Guider for Omnidirectional Image," IEEE Trans. Circuits Syst. Video Technol. **30**, 917–928 (2020).

[9] M. R. Miller, H. Jun, F. Herrera, J. Y. Villa, G. Welch, and J. N. Bailenson, "Social interaction in augmented reality," PLOS ONE **14**, e0216290 (2019).

[10] D. Shin, "How does immersion work in augmented reality games? A user-centric view of immersion and engagement," Inf. Commun. Soc. **22**, 1212–1229 (2019).

[11] R. T. Azuma, "Making Augmented Reality a Reality," in *Imaging and Applied Optics 2017*, OSA Technical Digest (Online) (Optica Publishing Group, 2017), p. JTu1F.1.

[12] J. Kim, Y. Jeong, M. Stengel, K. Akşit, R. Albert, B. Boudaoud, T. Greer, J. Kim, W. Lopes, Z. Majercik, P. Shirley, J. Spjut, M. McGuire, and D. Luebke, "Foveated AR: dynamically-foveated augmented reality display," ACM Trans. Graph. **38**, 99:1-99:15 (2019).

[13] T. Hirzle, M. Cordts, E. Rukzio, J. Gugenheimer, and A. Bulling, "A Critical Assessment of the Use of SSQ as a Measure of General Discomfort in VR Head-Mounted Displays," in *Proceedings of the 2021 CHI Conference on Human Factors in Computing Systems*, CHI '21 (Association for Computing Machinery, 2021), p. 530:1-530:14.

[14] N. A. Dodgson, "Variation and extrema of human interpupillary distance," Proc. SPIE **5291**, 36–46 (2004).

[15] J. Schwiegerling, *Field Guide to Visual and Ophthalmic Optics* (SPIE, 2004).

[16] J. W. Goodman, *Introduction to Fourier Optics*, 3rd ed. (Roberts and Company Publishers, 2005).

[17] J. min Cho, Y. do Kim, S. H. Jung, H. Shin, and T. Kim, "78-4: Screen Door Effect Mitigation and Its Quantitative Evaluation in VR Display," SID Symp. Dig. Tech. Pap. **48**, 1154–1156 (2017).

[18] S. Reichelt, R. Häussler, G. Fütterer, and N. Leister, "Depth cues in human visual perception and their realization in 3D displays," Proc. SPIE **7690**, 76900B (2010).

[19] H. Hua, "Enabling Focus Cues in Head-Mounted Displays," Proc. IEEE **105**, 805–824 (2017).

[20] K. J. MacKenzie, D. M. Hoffman, and S. J. Watt, "Accommodation to multiple-focal-plane displays: Implications for improving stereoscopic displays and for accommodation control," J. Vis. **10**, 22 (2010).

[21] R. Zabels, K. Osmanis, M. Narels, U. Gertners, A. Ozols, K. Rūtenbergs, and I. Osmanis, "AR Displays: Next-Generation Technologies to Solve the Vergence–Accommodation Conflict," Appl. Sci. **9**, 3147 (2019).

[22] D. M. Hoffman, A. R. Girshick, K. Akeley, and M. S. Banks, "Vergence–accommodation conflicts hinder visual performance and cause visual fatigue," J. Vis. **8**, 33 (2008).

[23] G. Kramida, "Resolving the Vergence-Accommodation Conflict in Head-Mounted Displays," IEEE Trans. Vis. Comput. Graphics **22**, 1912–1931 (2016).

[24] H. Huang and H. Hua, "High-performance integral-imaging-based light field augmented reality display using freeform optics," Opt. Express **26**, 17578–17590 (2018).

[25] X. Wang and H. Hua, "Depth-enhanced head-mounted light field displays based on integral imaging," Opt. Lett. **46**, 985–988 (2021).

[26] A. Maimone, A. Georgiou, and J. S. Kollin, "Holographic near-eye displays for virtual and augmented reality," ACM Trans. Graph. **36**, 85:1-85:16 (2017).

[27] S. B. Kim and J. H. Park, "Optical see-through Maxwellian near-to-eye display with an enlarged eyebox," Opt. Lett. **43**, 767–770 (2018).

[28] T. Zhan, J. Xiong, J. Zou, and S. T. Wu, "Multifocal displays: review and prospect," PhotoniX **1**, 10 (2020).

[29] J. Miseli, "7.3: Motion Artifacts," SID Symp. Dig. Tech. Pap. **35**, 86–89 (2004).

[30] B. Shneiderman, "Response time and display rate in human performance with computers," ACM Comput. Surv. **16**, 265–285 (1984).

[31] H. Pan, X. F. Feng, and S. Daly, "LCD motion blur modeling and analysis," in *IEEE International Conference on Image Processing 2005* (2005), **2**, p. II–21.

[32] J. Zhao, R. S. Allison, M. Vinnikov, and S. Jennings, "Estimating the motion-to-photon latency in head mounted displays," in *2017 IEEE Virtual Reality (VR)* (2017), pp. 313–314.

[33] P. Lincoln, A. Blate, M. Singh, T. Whitted, A. State, A. Lastra, and H. Fuchs, "From Motion to Photons in 80 Microseconds: Towards Minimal Latency for Virtual and Augmented Reality," IEEE Trans. Vis. Comput. Graphics **22**, 1367–1376 (2016).

[34] H. Seetzen, W. Heidrich, W. Stuerzlinger, G. Ward, L. Whitehead, M. Trentacoste, A. Ghosh, and A. Vorozcovs, "High dynamic range display systems," ACM Trans. Graph. **23**, 760–768 (2004).

[35] P. Lincoln, A. Blate, M. Singh, A. State, M. C. Whitton, T. Whitted, and H. Fuchs, "Scene-adaptive high dynamic range display for low latency augmented reality," in *Proceedings of the 21st ACM SIGGRAPH Symposium on Interactive 3D Graphics and Games*, I3D '17 (Association for Computing Machinery, 2017), p. 15:1-15:7.

[36] Y. H. Lee, T. Zhan, and S. T. Wu, "Prospects and challenges in augmented reality displays," Virtual Real. Intell. Hardw. **1**, 10–20 (2019).

[37] S. A. Cholewiak, Z. Başgöze, O. Cakmakci, D. M. Hoffman, and E. A. Cooper, "A perceptual eyebox for near-eye displays," Opt. Express **28**, 38008–38028 (2020).

[38] E. Hecht, *Optics* (Pearson, 2017).

[39] T. Lin, T. Zhan, J. Zou, F. Fan, and S. T. Wu, "Maxwellian near-eye display with an expanded eyebox," Opt. Express **28**, 38616–38625 (2020).

[40] J. Xiong, Y. Li, K. Li, and S. T. Wu, "Aberration-free pupil steerable Maxwellian display for augmented reality with cholesteric liquid crystal holographic lenses," Opt. Lett. **46**, 1760–1763 (2021).

[41] K. Pulli, "11-2: Invited Paper: Meta 2: Immersive Optical-See-Through Augmented Reality," SID Symp. Dig. Tech. Pap. **48**, 132–133 (2017).

[42] B. Lee, C. Yoo, J. Jeong, B. Lee, and K. Bang, "Key issues and technologies for AR/VR head-mounted displays," Proc. SPIE. **11304**, 1130402 (2020).

[43] G. Westheimer, "The maxwellian view," Vis. Res. **6**, 669–682 (1966).

[44] C. Jang, K. Bang, S. Moon, J. Kim, S. Lee, and B. Lee, "Retinal 3D: augmented reality near-eye display via pupil-tracked light field projection on retina," ACM Trans. Graph. **36**, 190:1-190:13 (2017).

[45] D. Cheng, Y. Wang, H. Hua, and M. M. Talha, "Design of an optical see-through head-mounted display with a low f-number and large field of view using a freeform prism," Appl. Opt. **48**, 2655–2668 (2009).

[46] G. Haas, "52-1: Invited Paper: Microdisplays for Wearable Augmented Reality — OLED vs LED Based Systems (Invited)," SID Symp. Dig. Tech. Pap. **50**, 713–716 (2019).

[47] Z. Chen, S. Yan, and C. Danesh, "MicroLED technologies and applications: characteristics, fabrication, progress, and challenges," J. Phys. D: Appl. Phys. **54**, 123001 (2021).

[48] Z. Zhang, Z. You, and D. Chu, "Fundamentals of phase-only liquid crystal on silicon (LCOS) devices," Light Sci. Appl. **3**, e213–e213 (2014).

[49] Y. Huang, E. Liao, R. Chen, and S. T. Wu, "Liquid-Crystal-on-Silicon for Augmented Reality Displays," Appl. Sci. **8**, 2366 (2018).

[50] Y. C. Huang and J. W. Pan, "High contrast ratio and compact-sized prism for DLP projection system," Opt. Express **22**, 17016–17029 (2014).

[51] Y. H. Ju, J. H. Park, J. H. Lee, J. Y. Lee, K. B. Nahm, J. H. Ko, and J. H. Kim, "Study on the Simulation Model for the Optimization of Optical Structures of Edge-lit Backlight for LCD Applications," J. Opt. Soc. Korea **12**, 25–30 (2008).

[52] T. Levola and P. Ayras, "Illumination of LCOS micro displays using planar lightguides," in *2008 2nd Electronics System-Integration Technology Conference* (2008), pp. 815–818.

[53] Y. W. Li, C. W. Lin, K. Y. Chen, K. H. Fan-Chiang, H. C. Kuo, and H. C. Tsai, "18.5L: Late-News Paper: Front-lit LCOS for Wearable Applications," SID Symp. Dig. Tech. Pap. **45**, 234–236 (2014).

[54] K. Y. Chen, Y. W. Li, K. H. Fan-Chiang, H. C. Kuo, and H. C. Tsai, "P-181L: Late-News Poster: Color Sequential Front-Lit LCOS for Wearable Displays," SID Symp. Dig. Tech. Pap. **46**, 1737–1740 (2015).

[55] J. Busch and G. Scheib, "Front lighting system for liquid crystal display," United States patent US5477239A (December 19, 1995).

[56] K. R. Curtis, B. J. SISSOM, H. C. Cheng, M. H. S. III, S. Bhargava, and E. H. Arend, "Waveguide illuminator," United States patent US20190179149A1 (June 13, 2019).

[57] K. R. Curtis, "Unveiling Magic Leap 2's Advanced AR Platform and Revolutionary Optics," Proc. SPIE. **11932**, 119320P (2022).

[58] E. Tang, "Smallest LED light engines for AR," Proc. SPIE. **11932**, 119321W (2022).

[59] F. Fidler, A. Balbekova, L. Noui, S. Anjou, T. Werner, and J. Reitterer, "Laser beam scanning in XR: benefits and challenges," Proc. SPIE. **11765**, 1176502 (2021).

[60] J. Reitterer, Z. Chen, A. Balbekova, G. Schmid, G. Schestak, F. Nassar, M. Dorfmeister, and M. Ley, "Ultra-compact micro-electro-mechanical laser beam scanner for augmented reality applications," Proc. SPIE. **11765**, 1176504 (2021).

[61] J. Reitterer, "Trixel® 3 – The world's smallest laser beam scanner for high-volume consumer augmented reality applications," Proc. SPIE. **11932**, 1193209 (2022).

[62] D. K. Yang and S. T. Wu, *Fundamentals of Liquid Crystal Devices* (John Wiley & Sons, 2014).

[63] W. R. Klein and B. D. Cook, "Unified Approach to Ultrasonic Light Diffraction," IEEE Transactions on Sonics and Ultrasonics **14**, 123–134 (1967).

[64] M. G. Moharam and L. Young, "Criterion for Bragg and Raman-Nath diffraction regimes," Appl. Opt. **17**, 1757–1759 (1978).

[65] J. Xiong and S. T. Wu, "Rigorous coupled-wave analysis of liquid crystal polarization gratings," Opt. Express **28**, 35960–35971 (2020).

[66] B. E. A. Saleh and M. C. Teich, *Fundamentals of Photonics* (John Wiley & Sons, 2019).

[67] Q. Yang, Z. Yang, Y. F. Lan, and S. T. Wu, "Low-diffraction transparent micro light-emitting diode displays with optimized pixel structure," J. Soc. Inf. Disp. **30**, 395–403 (2022).

[68] Y. Huang, E. L. Hsiang, M. Y. Deng, and S. T. Wu, "Mini-LED, Micro-LED and OLED displays: present status and future perspectives," Light Sci. Appl. **9**, 105 (2020).

[69] R. S. Cok, M. Meitl, R. Rotzoll, G. Melnik, A. Fecioru, A. J. Trindade, B. Raymond, S. Bonafede, D. Gomez, T. Moore, C. Prevatte, E. Radauscher, S. Goodwin, P. Hines, and C. A. Bower, "Inorganic light-emitting diode displays using micro-transfer printing," J. Soc. Inf. Disp. **25**, 589–609 (2017).

[70] Y. Huang, G. Tan, F. Gou, M. C. Li, S. L. Lee, and S. T. Wu, "Prospects and challenges of mini-LED and micro-LED displays," J. Soc. Inf. Disp. **27**, 387–401 (2019).

[71] Y. T. Liu, K. Y. Liao, C. L. Lin, and Y. L. Li, "66-2: Invited Paper: PixeLED Display for Transparent Applications," SID Symp. Dig. Tech. Pap. **49**, 874–875 (2018).

[72] G. Biwa, A. Aoyagi, M. Doi, K. Tomoda, A. Yasuda, and H. Kadota, "Technologies for the Crystal LED display system," J. Soc. Inf. Disp. **29**, 435–445 (2021).

[73] H. Kim, A. Miranda Anon, T. Misu, N. Li, A. Tawari, and K. Fujimura, "Look at Me: Augmented Reality Pedestrian Warning System Using an In-Vehicle Volumetric Head Up Display," in *Proceedings of the 21st International Conference on Intelligent User Interfaces*, IUI '16 (Association for Computing Machinery, 2016), pp. 294–298.

[74] J. L. Gabbard, G. M. Fitch, and H. Kim, "Behind the Glass: Driver Challenges and Opportunities for AR Automotive Applications," Proc. IEEE **102**, 124–136 (2014).

[75] S. Krotkus, D. Kasemann, S. Lenk, K. Leo, and S. Reineke, "Adjustable white-light emission from a photo-structured micro-OLED array," Light Sci. Appl. **5**, e16121–e16121 (2016).

[76] K. T. Chen, Y. H. Huang, Y. H. Tsai, W. C. Chen, L. H. Wang, H. Y. Chen, G. Chen, J. C. Ho, and C. C. Lee, "60-1: Invited Paper: Highly Transparent AMOLED Display with Interactive System," SID Symp. Dig. Tech. Pap. **50**, 842–845 (2019).

[77] Y. Zhou, D. Ren, N. Emerton, S. Lim, and T. Large, "Image Restoration for Under-Display Camera," in *2021 IEEE/CVF Conference on Computer Vision and Pattern Recognition (CVPR)* (IEEE Computer Society, 2021), pp. 9175–9184.

[78] Y. H. Tsai, M. H. Huang, W. de Jeng, T. W. Huang, K. L. Lo, and M. Ou-Yang, "Image quality affected by diffraction of aperture structure arrangement in transparent active-matrix organic light-emitting diode displays," Appl. Opt. **54**, E136–E145 (2015).

[79] Z. Qin, J. Xie, F. C. Lin, Y. P. Huang, and H. P. D. Shieh, "Evaluation of a Transparent Display's Pixel Structure Regarding Subjective Quality of Diffracted See-Through Images," IEEE Photonics Journal **9**, 7000414 (2017).

[80] Q. Yang, Y. Li, Y. Ding, and S. T. Wu, "Compact Foveated AR Displays with Polarization Selective Planar Lenses," ACS Appl. Opt. Mater. (2023).

[81] K. Yin, E. L. Hsiang, J. Zou, Y. Li, Z. Yang, Q. Yang, P. C. Lai, C. L. Lin, and S. T. Wu, "Advanced liquid crystal devices for augmented reality and virtual reality displays: principles and applications," Light Sci. Appl. **11**, 161 (2022).

[82] Y. Li, Q. Yang, J. Xiong, K. Yin, and S. T. Wu, "3D displays in augmented and virtual realities with holographic optical elements [Invited]," Opt. Express **29**, 42696–42712 (2021).

[83] G. Tan, Y. H. Lee, T. Zhan, J. Yang, S. Liu, D. Zhao, and S. T. Wu, "Foveated imaging for near-eye displays," Opt. Express **26**, 25076–25085 (2018).

[84] S. Lee, M. Wang, G. Li, L. Lu, Y. Sulai, C. Jang, and B. Silverstein, "Foveated near-eye display for mixed reality using liquid crystal photonics," Sci. Rep. **10**, 16127 (2020).

[85] P. Lyu and H. Hua, "Perceptual-driven approach to statically foveated head-mounted displays," Opt. Express **29**, 33890–33914 (2021).

[86] C. Yoo, J. Xiong, S. Moon, D. Yoo, C. K. Lee, S. T. Wu, and B. Lee, "Foveated display system based on a doublet geometric phase lens," Opt. Express **28**, 23690–23702 (2020).

[87] K. Yin, Z. He, Y. Li, and S. T. Wu, "Foveated imaging by polarization multiplexing for compact near-eye displays," J. Soc. Inf. Disp. **30**, 381–386 (2022).

[88] J. Kobashi, H. Yoshida, and M. Ozaki, "Planar optics with patterned chiral liquid crystals," Nature Photon. **10**, 389–392 (2016).

[89] P. Chen, B. Y. Wei, W. Hu, and Y. Q. Lu, "Liquid-Crystal-Mediated Geometric Phase: From Transmissive to Broadband Reflective Planar Optics," Adv. Mater **32**, 1903665 (2020).

[90] Y. Li, T. Zhan, and S. T. Wu, "Flat cholesteric liquid crystal polymeric lens with low f-number," Opt. Express **28**, 5875–5882 (2020).

[91] P. Chen, L. L. Ma, W. Hu, Z. X. Shen, H. K. Bisoyi, S. B. Wu, S. J. Ge, Q. Li, and Y. Q. Lu, "Chirality invertible superstructure mediated active planar optics," Nat. Commun. **10**, 2518 (2019).

[92] Y. H. Lee, K. Yin, and S. T. Wu, "Reflective polarization volume gratings for high efficiency waveguide-coupling augmented reality displays," Opt. Express **25**, 27008–27014 (2017).

[93] Y. Weng, Y. Zhang, J. Cui, A. Liu, Z. Shen, X. Li, and B. Wang, "Liquid-crystal-based polarization volume grating applied for full-color waveguide displays," Opt. Lett. **43**, 5773–5776 (2018).

[94] J. Kobashi, Y. Mohri, H. Yoshida, and M. Ozaki, "Circularly-polarized, large-angle reflective deflectors based on periodically patterned cholesteric liquid crystals," Optical Data Processing and Storage **3**, 61–66 (2017).

[95] J. Xiong, Q. Yang, Y. Li, and S. T. Wu, "Holo-imprinting polarization optics with a reflective liquid crystal hologram template," Light Sci. Appl. **11**, 54 (2022).

[96] S. R. Nersisyan, N. V. Tabiryan, D. M. Steeves, and B. R. Kimball, "Characterization of optically imprinted polarization gratings," Appl. Opt. **48**, 4062–4067 (2009).

[97] Y. Gu, Y. Weng, R. Wei, Z. Shen, C. Wang, L. Zhang, and Y. Zhang, "Holographic Waveguide Display With Large Field of View and High Light Efficiency Based on Polarized Volume Holographic Grating," IEEE Photonics Journal **14**, 7003707 (2022).

[98] Y. Li, Q. Yang, J. Xiong, K. Li, and S. T. Wu, "Dual-depth augmented reality display with reflective polarization-dependent lenses," Opt. Express **29**, 31478–31487 (2021).

[99] I. Nys, M. Stebryte, Y. Ye. Ussembayev, J. Beeckman, and K. Neyts, "Tilted Chiral Liquid Crystal Gratings for Efficient Large-Angle Diffraction," Adv. Optical Mater. **7**, 1901364 (2019).

[100] K. Yin, Z. He, and S. T. Wu, "Reflective Polarization Volume Lens with Small f-Number and Large Diffraction Angle," Adv. Optical Mater. **8**, 2000170 (2020).

[101] Q. Yang, Y. Ding, and S. T. Wu, "Full-color, wide FoV single-layer waveguide for AR displays," J. Soc. Inf. Disp. (2024).

[102] Y. Amitai, "P-21: Extremely Compact High-Performance HMDs Based on Substrate-Guided Optical Element," SID Symp. Dig. Tech. Pap. **35**, 310–313 (2004).

[103] B. C. Kress and I. Chatterjee, "Waveguide combiners for mixed reality headsets: a nanophotonics design perspective," Nanophotonics **10**, 41–74 (2021).

[104] D. Cheng, Q. Wang, Y. Liu, H. Chen, D. Ni, X. Wang, C. Yao, Q. Hou, W. Hou, G. Luo, and Y. Wang, "Design and manufacture AR head-mounted displays: A review and outlook," Light: Advanced Manufacturing **2**, 350–369 (2021).

[105] Y. Ding, Y. Li, Q. Yang, and S. T. Wu, "Design optimization of polarization volume gratings for full-color waveguide-based augmented reality displays," J. Soc. Inf. Disp. **31**, 380–386 (2023).

[106] B. C. Kress, "Optical waveguide combiners for AR headsets: features and limitations," Proc. SPIE. **11062**, 110620J (2019).

[107] J. Xiong, K. Yin, K. Li, and S. T. Wu, "Holographic Optical Elements for Augmented Reality: Principles, Present Status, and Future Perspectives," Adv. Photonics Res. **2**, 2000049 (2021).

[108] Y. Weng, D. Xu, Y. Zhang, X. Li, and S. T. Wu, "Polarization volume grating with high efficiency and large diffraction angle," Opt. Express **24**, 17746–17759 (2016).

[109] Y. Weng, Y. Zhang, W. Wang, Y. Gu, C. Wang, R. Wei, L. Zhang, and B. Wang, "High-efficiency and compact two-dimensional exit pupil expansion design for diffractive waveguide based on polarization volume grating," Opt. Express **31**, 6601–6614 (2023).

[110] Y. Li, J. Semmen, Q. Yang, and S. T. Wu, "Switchable polarization volume gratings for augmented reality waveguide displays," J. Soc. Inf. Disp. **31**, 328–335 (2023).

[111] D. J. Broer, J. Lub, and G. N. Mol, "Wide-band reflective polarizers from cholesteric polymer networks with a pitch gradient," Nature **378**, 467–469 (1995).

[112] M. Mitov, "Cholesteric Liquid Crystals with a Broad Light Reflection Band," Adv. Mater. **24**, 6260–6276 (2012).

[113] K. Yin, H. Y. Lin, and S. T. Wu, "Chirped polarization volume grating with ultra-wide angular bandwidth and high efficiency for see-through near-eye displays," Opt. Express **27**, 35895–35902 (2019).

[114] X. Yan, J. Wang, W. Zhang, Y. Liu, and D. Luo, "Gradient polarization volume grating with wide angular bandwidth for augmented reality," Opt. Express **31**, 35282–35292 (2023).